Utrecht University

Graduate School of Natural Sciences

MSc Climate Physics

Quantifying the influence of submesoscale processes on measured transport of floating plastic in the Great Pacific Garbage Patch

Author:
Mattia Romero

Supervisors:
Yannick Pham[1]
Dr. Laura Gómez Navarro[2]

Examiners:
Prof. dr. Erik van Sebille[2]
Dr. M.L.J. (Michiel) Baatsen[2]

August 4, 2023

Utrecht University

THE OCEAN CLEANUP™

[1]The Ocean Cleanup Foundation, Rotterdam, The Netherlands
[2]Institute for Marine and Atmospheric Research, Utrecht University, Utrecht, The Netherlands

Acknowledgments

I would like to thank first and foremost my family for the endless support throughout my student career, I would have not made it this far without them. A big thank you goes also to my course-mates and friends who kept the *master's room* a fun and stimulating environment, even through the rainiest and toughest winter days. Thanks Laura for the incredible academic and moral support, you've gone above and beyond, and thank you Erik for the continuous constructive criticism, your comments have allowed me to think more critically and delivering a better end result. Thank you Michiel for taking the time to read my thesis, amongst the many students that you have supervised this year. Last but definitely not least, I am extremely thankful to The Ocean Cleanup crew for having allowed me to embark on this adventure with them, with a special thank you going to Yannick and Robin, who have supported me through the many complexities of this project, as well as for the folks offshore who have bravely collected this data. This thesis would have literally not been possible without all of you.

Abstract

The Great Pacific Garbage Patch (GPGP) is known for accumulating floating plastic, but little is known on the dominating mechanisms that form its heterogeneity. Submesoscale processes are likely the main drivers of such heterogeneity, especially if their effect on transport is object-specific. This hypothesis is investigated by analysing shipboard remote sensing and metocean data. By developing a Particle Tracking Velocimetry (PTV) methodology, floating plastic's velocities are derived from GoPro and drone data collected during The Ocean Cleanup's operational and research campaigns. Research findings show that surface currents, without additional forcings, cannot fully account for more than half of the variance in floating plastic transport within the North-West region of the GPGP. This suggests that leeway, an important factor in floating plastic transport, is likely a non-negligible component for most items in the area, with varying leeway rates observed across the sample. Furthermore, an analysis on submesoscale accumulation indicates that density fronts may contribute to creating heterogeneity at smaller scales. Notably, two episodes demonstrate higher floating plastic accumulation along density fronts than in the surrounding environment. In summary, this study sheds light on the crucial role of submesoscale processes in shaping the heterogeneity of the Great Pacific Garbage Patch. Understanding these mechanisms can lead to more effective strategies for mitigating plastic pollution and its environmental impacts.

Contents

List of Abbreviations

Abbreviation	Meaning
DVL	Doppler Velocity Log
GPGP	Great Pacific Garbage Patch
Metocean	Meteorology and (physical) oceanography
NPM5	North Pacific Mission 5
PTV	Particle Tracking Velocimetry
SOG	Speed over ground
STW	Speed through water
SWH	Significant wave height
UAV	Unmanned Aerial Vehicle

Chapter 1

Introduction

Within the field of oceanography, the past decades have seen numerous publications exposing evidence on the effects of an ever growing consumerist society on the marine environment. It is not surprising that both the climate and plastic pollution crises go hand-in-hand, as they both develop from the same source: human activity. Although climate change remains the biggest threat to an already fragile and vulnerable marine ecosystem (UNESCO, 2021), plastic pollution, a human product for human, land-based consumption, reached as far as the most hostile and virgin environments of Antarctica (Aves et al., 2022). After years of research and careful monitoring fueled by media exposure, it is now well known that plastic pollution leaks from society into the marine environment primarily through its arteries: rivers (The Ocean Cleanup, 2023).

1.1 Ocean plastic

Out of the 400 million metric tons of yearly plastic production (OECD, 2022), approximately equivalent to the total human weight, it's likely that less than 1 % leaks into the ocean through waterways (Meijer et al., 2021). Once in the marine environment, plastic is subject to several physical, chemical and biological (through interaction with marine species) mechanisms that transport it and degrade it over time. Despite its known longevity, plastic eventually fragments, mainly through mechanical abrasion and exposure to UV radiation (van Sebille et al., 2020). There is no community-wide agreement on the appropriate definition of plastic size ranges in the literature. Therefore, following van Sebille et al. (2020)'s approach, size nomenclature in this study will refer what is used within the respective papers that are cited. Smaller size fragmented plastic accumulation may be particularly harmful for the environment, as it may more easily interact with more species and be ingested in larger quantities (Zolotova et al., 2022). Although life-threatening through physical damage, trapping, ingestion and chemical releases, little is still known on the effects of plastic pollution on the marine environment (IUCN, 2023).

Over the past decades, expertise from neighbouring fields, such as oil spill dispersion, marine search and rescue and biological connectivity, has been applied by oceanographers to better understand the ocean plastic pollution problem. Despite the recent progress in the field and depending on the frame of reference (item number or mass), quantification of plastic's distribution in the marine environment is still a source of disagreement in the scientific community (Eriksen et al., 2014; van Sebille et al., 2015; Lebreton et al., 2018; 2022; Kaandorp et al., 2023). What is known, is that the majority of plastic mass that does not sink, beach, or reside in the water column, can be subject to long-distance transport from source areas (Thompson et al., 2005) and accumulates primarily in large scale accumulation regions such as subtropical gyres (Wichmann et al., 2019). Based on several sources of evidence, the gyre with the highest surface density of floating plastic is the North Pacific Subtropical Gyre (Kaandorp et al., 2023; Onink et al., 2019; van Sebille et al., 2012). The Great Pacific Garbage Patch (GPGP) is a vast area within this gyre, known to be covered with tens of thousands of tonnes of floating plastic debris, spanning millions of square kilometres (Lebreton et al., 2022). Recent studies found that more than half of the plastic residing in the gyre is released from fishing activity (Lebreton et al., 2018). Fishing nets, ropes and other hard plastic objects (> 5 cm) sum up to three-quarters of the accumulated floating plastic mass in the region (Lebreton et al., 2022). These objects are less subject to degradation over time because of their nature, remaining afloat and hardly fragmenting (Lebreton et al., 2022). Due to their variety in density, shape and size, such items likely experience different dominant transport mechanisms (Ruiz et al., 2022). Beause the North Pacific Subtropical Gyre is known for having the highest concentrations of floating plastic, it has been targeted by cleanup efforts. Despite their remote location and the smaller biological activity compared to coastal areas (Hajbane et al., 2021), gyres are areas of cleanup interest because they are regions where plastic is hardly removed by physical mechanisms, as recently confirmed by Kaandorp et al. (2023). Cleanup efforts in this region have been conducted by The Ocean Cleanup, with a focus on larger floating items, hoping to limit plastic fragmentation and optimise catch (The Ocean Cleanup, n.d.).

1.2 The Ocean Cleanup

The Ocean Cleanup is a Dutch Foundation that focuses on downstream and upstream plastic pollution solutions. It currently conducts two types of downstream cleanup efforts. Cleanup at the source, through waterways intervention, and cleanup of the *legacy pollution* (The Ocean Cleanup, n.d.), targeting gyres (see figure 1.1). Cleanup operations in the GPGP have started in 2021 and have continued intermittently. Over this period extensive field measurements have been recorded, including shipboard camera footage of the sea surface and metocean observations. Better understanding of how plastic is transported, distributed and emitted is critical for mitigation or policy strategies. This is why The Ocean Cleanup is involved in scientific research. Alongside its operational cleanup campaign, The Ocean Cleanup organises research cruises, such as the North Pacific Mission 5 (NPM5) which is analysed in this study. Further information on the campaigns and the data collected are in section 3.2.

Figure 1.1: Floating plastic collected from the GPGP (The Ocean Cleanup, n.d.).

1.3 Research questions and motivation

Once plastic enters the ocean, it is transported and evolves over time, influenced by fluid dynamics processes at all scales, ranging from large scale (hundreds to thousands of kilometers), to turbulent mixing (millimeters to tens of meters) (Sutherland et al., 2023). Despite the most recent advancements in the dynamics of floating ocean plastic, many unknowns still limit the understanding of its distribution and transport at the large scale and particularly at the submesoscale level. Numerical simulations of global and regional dynamics are not sufficiently resolved to reproduce fluid motion at the submesoscale and smaller, which are may substantially influence the transport of particles (Hewitt et al., 2022). These non-resolved phenomena include submesoscale processes, fronts, wave and wind-driven transport, amongst others (Sutherland et al., 2023). To be accurately accounted for in large scale models, such processes are parameterized through the application of fluid mechanics theory in high-resolution computational fluid dynamics simulations and laboratory experiments (Rakotonirina et al., 2022; Westerkamp et al., 2023). In situ measurements also play an important role, by improving understanding of such phenomena. This study focuses on submesoscale dynamics of floating plastic that resides in the North-West region of the North Pacific Subtropical Gyre, using in situ remote sensing observations and particle tracking techniques. The size range of observed floating plastic is $a_{min} > 0.15m$, where a_{min} is the minor axis of the detected item. This size limitation is dependent on the specifics of the remote sensing measurement devices, as detailed in de Vries et al. (2021). For simplicity, this subset of plastic sizes will be summarised by the term *floating plastic* in the remainder of the report. Nonetheless, this is an important clarification, as the analysis only focuses on these size ranges and smaller items are expected to be subject to different transport mechanisms, as well as being spatially distributed differently (Klink et al., 2022). Overall, the study's objective is twofold. Firstly, to investigate how in situ data can help model floating plastic transport mechanisms, with a focus on leeway. Secondly, to understand the role of fronts in creating small scale accumulation. Obtaining information on the transport heterogeneity across different item types in the gyre and their spatial distribution at the small scale can help cleanup efforts through improved parametrisation and data-assimilated computational modelling. Overall, the following research questions will be tackled.

1. Is floating plastic transport in the North-West GPGP mainly surface current-driven?

2. What is the role of leeway on floating plastic transport in the North-West GPGP?

3. How homogeneous is the leeway rate of floating plastic in the North-West GPGP?

4. Does floating plastic accumulate along density fronts?

Research questions 1-3 are addressed in section 4.1 and research question 4 in section 4.2.

Chapter 2

Theory

2.1 Dynamics of floating plastic in ocean gyres

This section summarises the conceptual knowledge on the dynamics within gyres, with the main focus on the North Pacific Subtropical Gyre (figure 2.2). Whilst oceanic processes occur at various spatio-temporal scales, only some can be observed by ship-based measurements (figure 2.1), and have varying importance on surface transport. Out of the physical mechanisms that drive floating plastic transport, this study focuses on the role of wind and waves, as well as fronts and eddy-induced small scale convergence. The focus is justified by the importance of these mechanisms on near-surface current shear within the upper metre of the water column. This suggests that larger items drift primarily due to wind and wave-induced motions (van Sebille et al., 2020), but in the absence of winds or waves, oceanic structures like eddies and fronts can also play an important role (Hajbane et al., 2021; Suaria and Aliani, 2022). When referring to surface transport, a clear definition of *surface current* needs to be stated for clarity. As argued by van der Mheen et al. (2020), the region of interest for floating material transport is the region between the air-sea interface (millimeters thick) that is dominated by viscous effects and the Ekman layer. There, the ocean current consists of: geostrophic currents, tidal currents, assorted baroclinic currents, Stokes drift, and wind-induced shear currents (Fernández and Pingree, 1996). Following van der Mheen et al. (2020) and Laxague et al. (2018), geostrophic, tidal, and baroclinic currents are defined as *background currents*. Stokes drift and the wind-induced shear current together make up the *drift current* described in section 4.1.2.

When considering a horizontal flow field, vorticity describes rotation in the vertical direction (Cushman-Roisin and Beckers, 2011). Relative vorticity is the component of vorticity with respect to the earth's rotation and it is computed as follows:

$$\zeta_z = \nabla_z \times \mathbf{u} = \frac{\partial u_y}{\partial x} \frac{\partial u_x}{\partial y} \tag{2.1}$$

The ratio between relative and planetary rotation, also known as Rossby number, is expressed as:

$$R_o = \frac{\zeta_z}{f} \tag{2.2}$$

When a Rossby number is much less than unity, the relative vorticity is negligible compared to the ambient vorticity, f, and geostrophic approximation is applicable (Cushman-Roisin and Beckers, 2011). In a rotating system, large-scale fluid motion can be conceptually interpreted as geostrophic flow (Cushman-Roisin and Beckers, 2011). Such flow is horizontally non-divergent by definition (Onink et al., 2019), as it moves along isobars. Hence, geostrophy contributes to surface transport, but cannot create accumulation. A non-divergent horizontal flow is expressed as $\delta_z = 0$, where divergence, δ_z, is defined as:

$$\delta_z = \nabla_z \mathbf{u} = \frac{\partial u_x}{\partial x} - \frac{\partial u_y}{\partial y} \tag{2.3}$$

Wind induces surface transport by deflection of surface currents, wave creation and through direct wind drag acting on the exposed section of the item of interest, if it is sufficiently buoyant. In combination with geostrophic currents, wind is the cause of large-scale accumulation of floating material through convergence.

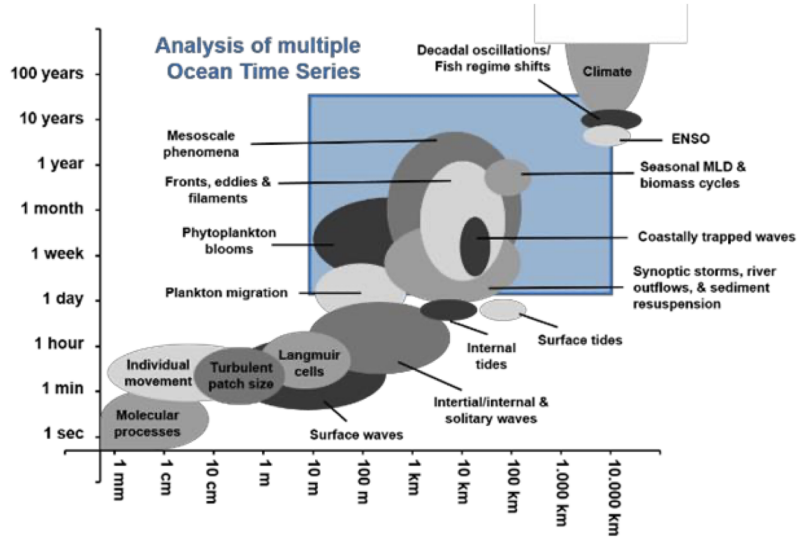

Figure 2.1: Schematic diagram with temporal and spatial scales of oceanic processes (O'Brien et al., 2017). The blue square highlights the range of spatial and temporal scales that can be addressed through ship-based, time-series measurements.

2.1.1 Wind

Large-scale circulation in the North Pacific Subtropical Gyre is driven by two prevailing winds: the Trade Winds and the Westerlies. The Trade Winds blow from North-West in the northern hemisphere and are generated by the pressure difference between the subtropical high-pressure and the equatorial low-pressure systems (Andrews, 1956). The Westerlies blow from West in the mid latitudes and are driven by the pressure difference between the subtropical high-pressure and the sub polar low-pressure systems (Andrews, 1956). The gyre is created by the interaction between geostrophy and the physical mechanism named Ekman transport.

Ekman transport

Large-scale surface convergence is caused by the deflection of near-surface winds due to the friction between the two fluids (wind-induced surface drag), with the direction of deflection that is dependent on the hemisphere under consideration. Such deflection is known as Ekman transport, and it expands downwards in the upper 10s of meters, forming a spiral with decreasing amplitude (Price et al., 1987). At the surface, Ekman transport is at approximately 45° with respect to the isobars. Ekman transport justifies the existence of subtropical gyres, which are large-scale areas of convergence, and their surface accumulation of floating material that does not experience waves or wind-induced drag (van Sebille et al., 2020). The Ekman and geostrophy-driven large-scale anticyclonic circulation in the North Pacific Subtropical Gyre is displayed in figure 2.2. The effects of Ekman transport on floating material is dependent on the vertical profile of the individual items, with thinner items subject to a smaller deflection angle, as confirmed by a study comparing drogued and non-drogued drifters' deflection angle (Rio and Piollé, 2015), amongst others. Onink et al. (2019) ran simulations with varying input currents, to investigate which transport mechanism best replicates accumulation of floating microplastic in the North Pacific. Simulations with Ekman currents (reported in green in figure 2.2) seem the best at replicating strong peaks in concentration of floating debris in the North Pacific subtropics (Onink et al., 2019). These results remark the importance of Ekman transport in explaining large-scale accumulation of floating material.

Windage

Windage is the direct effect of wind forcing on the buoyant component of floating material above the sea surface. In fluid mechanics, it is further broken down into skin friction drag, from the viscous friction on the object's surface (due to microscale roughness elements), and form drag, from the wind pressure on an obstacle (Petty et al., 2017; Kean and Smith, 2006). The latter is related to object size, shape and density through the buoyancy ratio (Zambianchi et al., 2014), R_A in equation 2.5. Due to the wide variety of floating items, windage is often parameterised in plastic dispersion models (Lebreton et al., 2018; Maximenko et al., 2018; Quoc et al., 2013). It is empirically expressed in the definition of the drift velocity component of the total velocity vector, $\mathbf{u}(\mathbf{x}, t)$, as a percentage of the wind speed as follows (Allshouse et al., 2016):

$$\mathbf{u}(\mathbf{x}, t) = \mathbf{u}_c(\mathbf{x}, t) + C_w \mathbf{u}_w(\mathbf{x}, t) \tag{2.4}$$

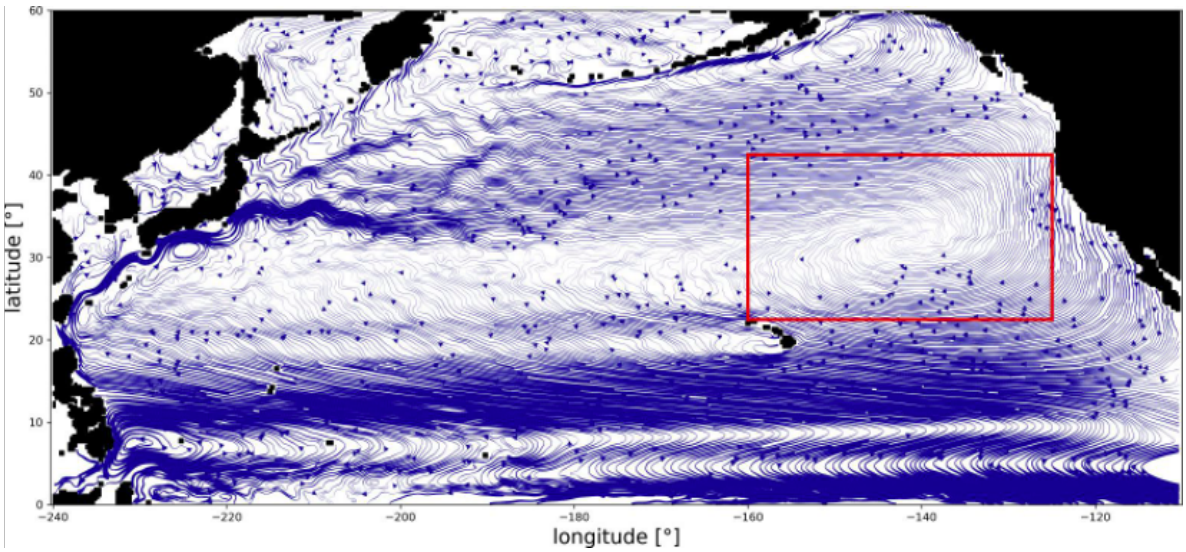

(a) 20 years average of daily mean geostrophic plus Ekman current velocities for the period 2000-2019 from Kunz (2023). It was computed by Kunz (2023) from CMEMS (copernicus-globcurrent) surface velocity data.

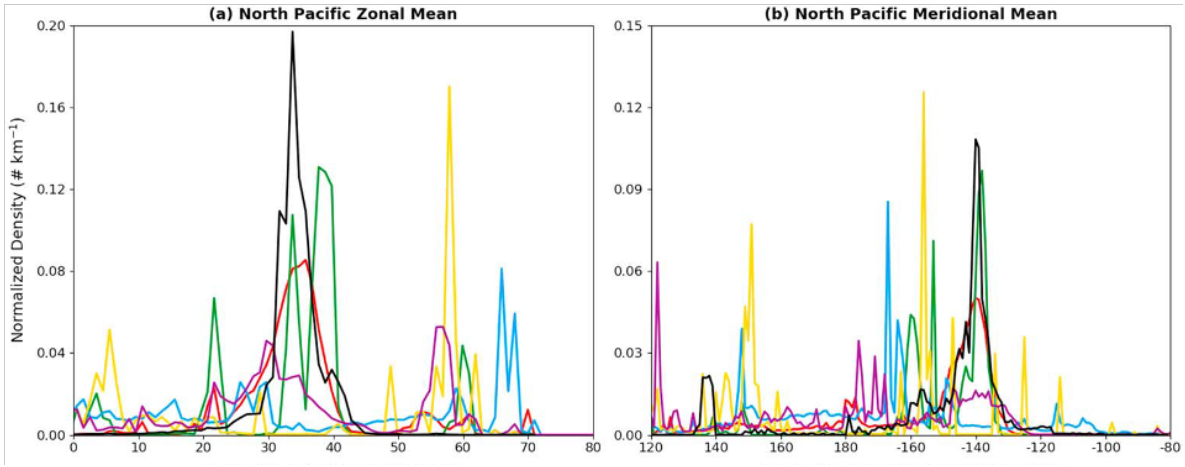

(b) Normalised zonal and meridional spatial means of observed and modeled microplastic concentrations with various daily mean surface current components for the North Pacific from Onink et al. (2019). Total (Ekman + geostrophic) in red, Ekman in green, geostrophic in blue, Stokes in yellow, Total + Stokes in purple and observations in black.

Figure 2.2: Ekman transport of floating debris in the North Pacific Subtropical Gyre.

where $\mathbf{u}_c(\mathbf{x}, t)$ is the current velocity, $\mathbf{u}_w(\mathbf{x}, t)$ is the wind velocity at 10 meters, by convention, and C_w is the windage coefficient, normally between 1 and 4% (van Sebille et al., 2020). C_w is further broken down following Richardson (1997) into:

$$C_w = \sqrt{\frac{\rho_{\text{air}}}{\rho_{\text{water}}}}\sqrt{\frac{C_{\text{air}}}{C_{\text{water}}}}\sqrt{\frac{A_{\text{air}}}{A_{\text{water}}}} = R_\rho R_C R_A \tag{2.5}$$

where, R_ρ is the ratio of the fluid densities, ρ_{air} and ρ_{water}. R_C is the ratio of the drag coefficients, C_{air} and C_{water}, on the over-water and submerged parts of the object, respectively. R_A is the buoyancy ratio, with A_{air} and A_{water} the emerged area and the submerged areas perpendicular to the wind flow of the object. Although questionable, a drag coefficient ratio $R_C = 1$ is often assumed (van der Mheen et al., 2020). R_ρ can also be assumed constant within the same region (van der Mheen et al., 2020), leaving C_w dependent on R_A. Evidence from in situ measurements (Allen and Plourde, 1999; Breivik et al., 2011) shows that direct wind-induced drag is non-negligible in the transport of floating material in the ocean. Nonetheless, it is often the case in the Lagrangian literature (Lebreton et al., 2018; 2022; Quoc et al., 2013) that surface dynamics of floating material in subtropical gyres are simplified by neglecting windage. In principle, this simplification is valid and justified when the goal is to study accumulation rates of fully submerged objects, as items with low to no wind-drag are more likely to accumulate in areas of surface convergence (Lebreton et al., 2018). However, when analysing transport mechanisms from observations at one point in time, such simplification is inadequate, as items with high windage that are travelling through the gyre may be spotted. This finding is supported by several modeling and laboratory studies, as well as evidence from the transport of floating debris originated from the 2011 Tohoku tsunami in Japan (Maximenko et al., 2018). Direct wind drag may be responsible for sorting plastic items with different buoyancy and size. Indeed, their wind drag coefficient influences their dispersion, ultimately affecting both residence time and beaching characteristics of floating items (Zambianchi et al., 2014). Overall, the influence of object shape, size, and density on windage is obvious from a theoretical standpoint; however, accurate simulations require field sampling and laboratory measurements.

2.1.2 Waves

Wind is also the cause of waves through friction. A wave regime refers to the prevailing sea conditions at a specific place and time. It encompasses two categories of wind-generated gravity waves: swell and wind sea. Swell originates at a distance from the observed area and generally carries minimal energy from the local wind (Villacieros-Robineau et al., 2021). Waves are another important transport mechanism of floating material through Stokes drift. Waves' periodicity induces a net drift velocity of floating material in the direction of wave propagation through signal asymmetry along its vertical profile. This phenomenon is called Stokes drift (Stokes, 1847). In average terms, it is the difference between the Lagrangian flow velocity of a fluid particle and the Eulerian flow velocity of the fluid as a whole (van den Bremer and Breivik, 2018). In mixed swell and wind wave regimes, which is often the case, the full two-dimensional wave spectrum must be represented for a complete computation

of Stokes drift (van den Bremer and Breivik, 2018). Nonetheless, Clarke and Gorder (2018) remark that since Stokes drift is proportional to wave frequency cubed, its magnitude depends strongly on the high-frequency tail of the spectrum: wind waves. They found correlations of surface Stokes drift with local wind stress, formulating a quantitative relationship. Wind waves often propagate in the same direction as the wind hence, enhancing floating material's drift through the added Stokes drift. Lagrangian simulations show the importance of this mechanism in transporting floating material to areas where it could not arrive only through wind and current-induced transport (Onink et al., 2019; Dobler et al., 2019). Due to its relevance in transport, recent findings have focused on the role of wave-induced drift for different object shapes, sizes and densities (Alsina et al., 2020; Di Benedetto et al., 2022; Santamaria et al., 2013; Westerkamp et al., 2023). Indeed, large floating plastic items cannot be simplified as non-inertial passive tracers carried by their surrounding fluid (Sutherland et al., 2023). Numerical and analytical studies have shown the role of inertia in altering Stokes drift on floating objects (Di Benedetto et al., 2022; Santamaria et al., 2013). Furthermore, non-spherical objects introduce additional complexity through the time-evolving stresses acting on the surface (Sutherland et al., 2023). Therefore, it's likely that Stokes drift may not fully express the wave-induced drift across all floating plastic types.

2.1.3 Leeway

Overall, the implementation of wave-induced drift in Lagrangian modelling frameworks is still up for debate, due to its object specificity, as well as the correlation between wind and waves products. For this reason, simulations often under- or overestimate drift effects (Onink et al., 2019). Furthermore, Breivik et al. (2011) suggest that wave drift forces on small objects (< 30 m) can be neglected compared to wind forces as soon as the wave length is more than about six times the object's length. A compromise that some authors found is to neglect Stokes drift and instead artificially increase windage (Klink et al., 2022). The effects of wind and wind wave-induced motion of a drifting object relative to the surface current are often combined in the term *leeway* (van Sebille et al., 2020). More precisely, following the definition put forward by Allen and Plourde (1999):

Leeway is the motion of the object induced by wind (10 m reference height) and waves relative to the ambient current (between 0.3 and 1.0 m depth).

This is because in most cases both act in the same direction, as in situ observations found that the angular difference between the wind and wave propagation direction is smaller than $\pm$ 10° (Clarke and Gorder, 2018). It is thus practical in operational language to use the definition of leeway, which does not distinguish between the wind and the wave influence (Allen and Plourde, 1999). In the literature, leeway rate, L_r is defined as:

$$L_r = \frac{||\mathbf{L}(\mathbf{x}, t)||}{||\mathbf{u}_w(\mathbf{x}, t)||} \tag{2.6}$$

where, $\mathbf{u}_w(\mathbf{x}, t)$ is the wind velocity vector adjusted to 10 m height and $\mathbf{L}(\mathbf{x}, t)$ is the leeway

vector. Leeway can be separated into downwind, DWL and crosswind, CWL, components:

$$\mathbf{DWL} = |\mathbf{L}(\mathbf{x}, t)| \sin(90^\circ - L_\alpha) \tag{2.7}$$

$$\mathbf{CWL} = |\mathbf{L}(\mathbf{x}, t)| \cos(90^\circ - L_\alpha) \tag{2.8}$$

where L_α is the angle between the wind and the leeway direction. The leeway vector is ideally computed directly from devices attached to the object of interest (Breivik et al., 2011). Indirect methods instead, compute the leeway based on measurements made by a nearby current meter. Indirect methods are simpler to implement but more prone to measurement errors due to the distance of the measurement devices from the object (Breivik et al., 2011). A visual interpretation of cross and downwind leeway is presented in figure 2.3. They are the derived perpendicular and parallel components of leeway, respectively and they are derived from the measured leeway vector. Equation 2.4 can be rewritten to take into account the wind wave-induced drift:

$$\mathbf{u}(\mathbf{x}, t) = \mathbf{u}_c(\mathbf{x}, t) + L_r \mathbf{u}_w(\mathbf{x}, t) \tag{2.9}$$

where the leeway component consists of the windage and Stokes drift components, respectively, as follows:

$$L_r \mathbf{u}_w(\mathbf{x}, t) = C_w \mathbf{u}_w(\mathbf{x}, t) + \mathbf{u}_s(\mathbf{x}, t) \tag{2.10}$$

and where L_r is expressed by (Breivik et al., 2011) as a function of R_A, exactly like the windage coefficient in equation 2.5.

Following Allen and Plourde (1999)'s approach, leeway effects are assessed separately in cross and downwind components. This split helps differentiate transport mechanisms because the downwind component tends to follow an almost linear relationship with the wind speed and this allows a separate analysis of the crosswind component (Allen and Plourde, 1999). Downwind leeway is expected to be the highest magnitude component, whilst crosswind leeway is less straightforward, as it is dependent on the object's vertical profile and on the symmetry of its buoyant section (Breivik et al., 2011). Furthermore, objects' shapes on the water surface vary over time, as they move over three dimensions due to the current, wave and wind motion (Allen and Plourde, 1999). Additionally, leeway is best measured at high wind speeds, as the variance of the leeway angle increases with decreasing wind speed, making it a non-stationary statistic which is difficult to work with (Breivik et al., 2011). From now on, this study will adopt the leeway terminology for simplicity and due to the lack of more precise direct measurements that allow distinction between wave and wind induced drift. Other than

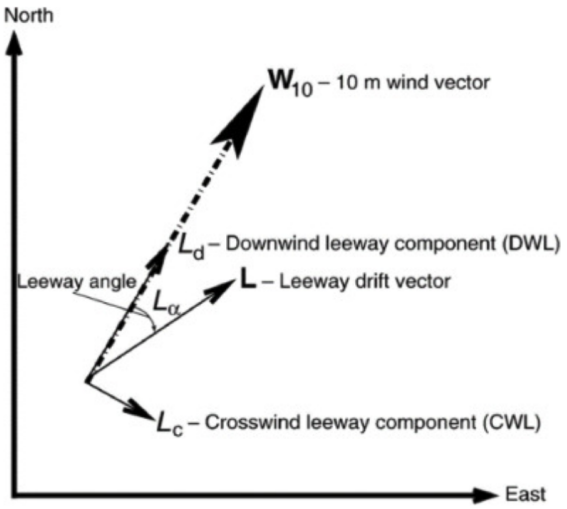

Figure 2.3: Visualisation of leeway in cross and downwind components (Quoc et al., 2013). Here, $\mathbf{u}_w$ is expressed as $\mathbf{W}_{10}$.

the benefit of a stronger and easier to detect signal, there are multiple drawbacks to this approach, such as the inability to separate wind and wave-induced drift, which are mentioned in detail in chapter 5. Above all, this simplification ignores the role of wave-induced drift in directions different to the wind vector, which may be particularly relevant for larger objects, as described in section 2.1.2.

2.1.4 Density fronts

Whilst Ekman currents drive large-scale accumulation of floating items (with low leeway rates) in regions of surface convergence, several other small-scale physical processes, that lead to convergent flows, explain accumulation at the meso- and submesoscale (Sutherland et al., 2023). Convergent flows occur along fronts which, by definition, are a region of significantly higher spatial rate of change of a physical property when compared to their surrounding (Belkin et al., 2009). The lateral density gradients across fronts are a source of potential energy (D'Asaro et al., 2018). There, the circulation is a single overturning cell with surface divergence where the lighter fluid is located and surface convergence on the dense side (D'Asaro et al., 2018). Buoyant items accumulate along the boundary of convergent regions, as they cannot sink through downwelling (van Sebille et al., 2020) (see figure 2.4). Fronts vary substantially both spatially and temporally, they arise mostly near the top and bottom boundaries (Nikurashin and Ferrari, 2011) and can be just a few hundred meters wide (Sutherland et al., 2023).

Submesoscale currents emerge from mesoscale eddies and boundary currents. They exhibit scale ranges spanning from 0.1 to 10 kilometers in the horizontal dimension and 0.01 to 1 kilometer in the vertical dimension and they typically persist for hours to days in time (McWilliams, 2016). They are larger than turbulent isotropic currents, but smaller than the baroclinic deformation radius (McWilliams, 2016). Submesoscale currents' surface divergence, δ, and vertical vorticity, ζ, are at least of the same order of magnitude of the Coriolis frequency,

f, such that the Rossby number of deformation, $R = \frac{\zeta}{f}$, is of $O(1)$. Consequently, they are classified as non-geostrophic in dynamical terms.

When examining plastic transport at scales smaller than tens of kilometers, particle resolving simulations are not possible (Sutherland et al., 2023). Classical dispersion models treat the spread of floating material as a random process governed by scale-dependent horizontal diffusion LaCasce (2008). Hence, these models can only predict the average concentration and cannot explain much of the small-scale accumulation structures of floating material (D'Asaro et al., 2018). Great recent progress in modeling submesoscale ocean processes shows surface convergence forming at these scales along fronts (Hamlington et al., 2014; Sullivan and McWilliams, 2018; Xiu et al., 2022). Xiu et al. (2022) noticed significant concentrations of chlorophyll in patches located at the boundary between mesoscale eddies, surpassing the levels observed within the cyclonic eddy core. This boundary region, also known as the edge region, exhibits a horizontal density gradient and is analogous to a front (Callbeck et al., 2017). Through high resolution Lagrangian simulations, Xiu et al. (2022) conclude that this edge region between eddies experiences intense vertical motions. This finding aligns with the suggestion by Klein and Lapeyre (2009), who propose that the vertical exchange at the eddy edge could facilitate more efficient vertical exchanges, compared to the eddy center. Furthermore, in eddy structures, surface convergence strength depends on the Rossby number of deformation (Chen and Chen, 2023). Whilst mesoscale mechanisms drive upwelling in cyclones and downwelling in anticyclones (McGillicuddy et al., 1998), Liu et al. (2017) suggested that high concentration at the periphery of anticyclonic eddies could be induced by the ageostrophic secondary circulation. At the submesoscale, D'Asaro et al. (2018) found that density fronts and cyclonic vortices can be strong attractants of floating material through vortex stretching, as they measured a large number of drifters gathered into a single cluster less than 100 m wide.

Most fronts are quasi-stationary and recurrent (Belkin et al., 2009), meaning that they behave as if they were in equilibrium under defined circumstances. Due to their quasi-stationarity and relevance for surface accumulation, they are a relevant structure for the forecasting of accumulation areas of floating material.

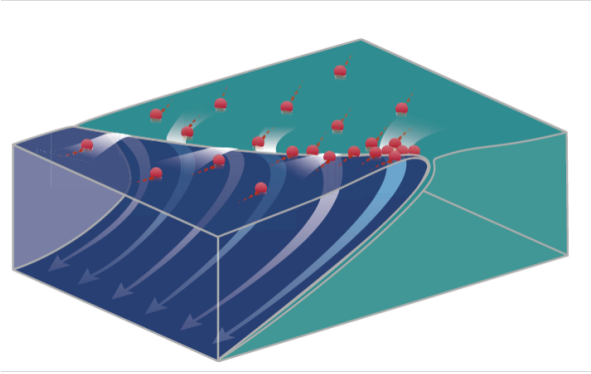

Figure 2.4: Visualisation of a density front (D'Asaro et al., 2018). The denser water mass downwells at the interface with the less dense mass, and accumulates floating material in doing so.

2.2 Distribution of floating plastic in the GPGP

Section 2.1 has outlined some of the most relevant mechanisms that drive transport and, therefore, distribution of floating plastic in ocean gyres. Depending on the spatial scale of analysis, some mechanisms will be more or less dominant.

2.2.1 Type distribution

Like any other material located at the boundary between atmosphere and ocean, as previously mentioned in section 2.1.1, plastic type will have an important impact on its transport. A good understanding of size range distribution is therefore crucial both for environmental impact assessment and for accurate spatial distribution forecasting. Lebreton et al. (2018) found that over three quarters of the GPGP's floating plastic mass was contained in the upper size classes (> 5 cm). Furthermore, they found that plastic type distribution was almost evenly distributed between hard (fragments and objects made of hard plastic) and soft (nets, ropes and lines) plastic. To give an example on the relevance of this information, consider large ropes and nets, which on average present a longer vertical profile and a smaller emerged area than hard plastic. This entails that they are less wind driven, and subject to Ekman transport at a different angle of deflection, similarly to drogued drifters. This is because the angle of deflection with respect to surface currents is determined by the Ekman spiral and so, it varies as the vertical profile increases (Price et al., 1987). During strong wind regimes, they could be travelling at an angle of up to 90° when compared to highly wind-driven items.

2.2.2 Spatial distribution

Floating plastic densities across the vast area of the GPGP are known to be heterogeneous Lebreton et al. (2018). Spatial distribution of floating plastic in the GPGP is mainly inferred from global and regional Lagrangian simulation outputs, as field sampling campaigns are too spatially constrained to draw region-wide conclusions. Spatial distribution is of course sensitive to release location, which is particularly relevant for the GPGP, as recent findings estimate that the majority of floating plastic in the area comes fishing activity (Lebreton et al., 2022). Nonetheless, as most items reside in the area for a long time, the distribution is mainly driven by the transport mechanisms that have been listed in section 2.1. Both Onink et al. (2019) and Lebreton et al. (2018) claim that low to null windage is the scenario that best represented measured plastic concentrations gradients, as well as inspection from trawl samples. Furthermore, Lebreton et al. (2018) hypothesizes that wind influence increases as the orbits around the patch become wider. This is because objects subject to greater atmospheric drag are more likely to escape the convergent zone. Hence, the dynamics of the gyre may act as filters of object type, with capacity to persist at the sea surface for extended periods of time and accumulate in ocean gyres, depending on their physical characteristics (Lebreton et al., 2018).

Chapter 3

Data and Methodology

The methodology developed in this study is a 2D application of Particle Tracking Velocimetry (PTV) on floating marine debris using optical cameras. PTV is a measuring technique in fluid mechanics used to derive velocities from trajectories of moving objects that are suspended in fluid flow (Dabiri and Pecora, 2019). It does so by tracking items in consecutive image frames and then computing the displacement vector for each successfully matched item. The core of PTV is correct particle identification and determination of its position in time (Dracos, 1996). This study's objective is applying PTV to derive floating plastic's point velocities at a location and time from short-term trajectory tracking using shipboard optical cameras. It is built as an extension to the ship-based optical remote sensing and artificial intelligence methodology used by de Vries et al. (2021) and recently improved by the same authors. The steps of the method are presented in this section and summarised in the workflow chart in figure 3.1. This study applies steps 1-4 from previous work and developed steps 5-9 from scratch. Steps 1 to 4 extract geolocation of detected objects from images. Once the tracking algorithm is applied (step 5), additional steps are introduced due to the challenges of implementing PTV on shipboard cameras (Schwendeman and Thomson, 2014). Manual validation (step 6) is conducted for quality control of the developed tracking algorithm, given the small sample size and its first use. Inaccuracies in geolocation due to the ship's movement limit the precision of PTV (Dracos, 1996). In step 7, a Monte Carlo analysis is conducted to estimate the variability in velocity derivation for different sea states and camera setups, which influence step 4 (Schwendeman and Thomson, 2014). Monte Carlo experiments are a common tool in quantitative scientific fields used to predict possible outcomes of an uncertain event by predicting a range of outcomes based on varying inputs (Johansen, 2010). Filtering techniques that reduce the noise signal are necessary to infer on the physical mechanisms driving the transport of the detected objects. These are applied in step 8, based on the Montecarlo analysis. The final subsection of this chapter is dedicated to step 9, which is the validation. Areas of overlapping Unmanned Aerial Vehicle (UAV) footage are used as secondary measurement device for assessment of the accuracy of the developed methodology.

Supporting maritime and metocean data is also presented in this chapter, as well as the

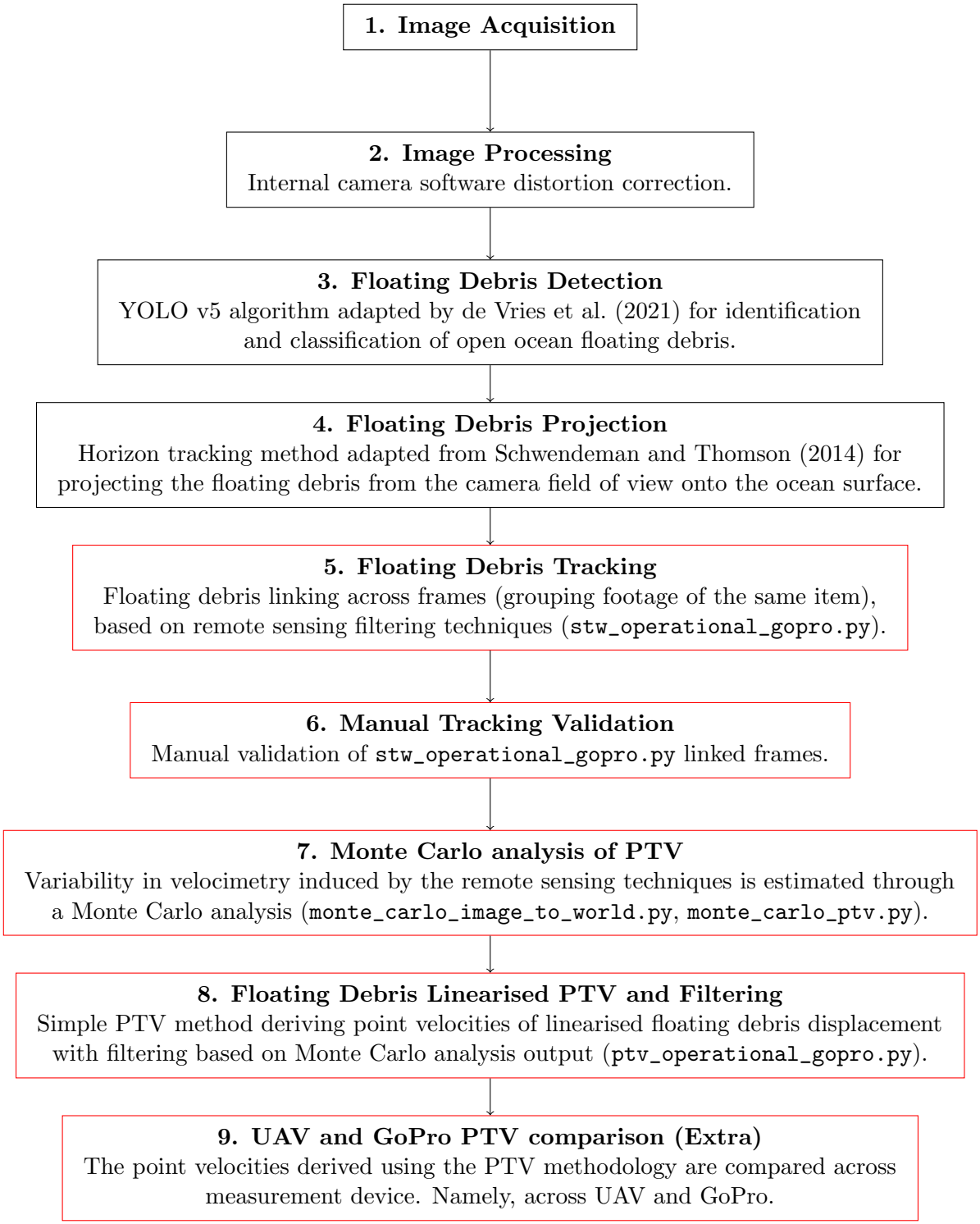

Figure 3.1: Workflow chart for PTV. The name of the scripts are reported in brackets for repeatability. Steps in red are product of the author. Step 5 was customised from existing script.

necessary post-processing and computational steps. The data used in this study comes from two sources: the research and operational field campaigns from the Ocean Cleanup (see section 1.2). NPM5, the research campaign analysed in this study, took place between 20/07/2022 and 03/08/2022, with the objective of spotting fronts and collecting samples of floating debris, as well as comparing results obtained from Schwendeman and Thomson (2014)'s camera setup with de Vries et al. (2021)'s. This dataset has two purposes in this study. It is used for validation of the method described in section 3.4, due to availability of overlapping UAV footage. Additionally, it is used to investigate the role of density fronts in accumulating floating plastic in section 4.2. This analysis is possible on the NPM5 dataset because of the presence of a thermosalinograph onboard, as well as a manually validated dataset of floating plastic counts, detected from shipboard cameras as detailed in section 3.3. The operational dataset created for this study is the 2022 section of the operations, spanning intermittently from May to December. This dataset is used for the analysis of plastic transport mechanisms due to larger sample size, distribution and availability of metocean measurement devices (anemometer, X-band radar), as detailed in section 3.2. Sections 3.2.1 and 4.1.1 explain the details of ship motion and surface current data for both campaigns. Sections 3.2.4 and 3.2.3 describe wind and wave data and are only applicable to the operational campaign, whilst section 3.2.5 describes the thermosalinograph data from NPM5.

Whilst the metocean data from the operational campaign was delivered to the author almost fully post-processed, the NPM5 data has been built from scratch from the raw measurement devices log files, following the procedures mentioned in section 3.2. Any error in the data from section 3.2 is therefore attributed to the author.

3.1 GoPro Setup (optical remote sensing)

To track floating marine debris, shipboard optical remote sensing cameras are used in both campaigns analysed this study. All shipboard cameras are GoPro® Hero 6 Black, set to 4K resolution. The data inputs are frames of the water surface from cameras clamped to the ship starboard- and port-side railings at height and angle that optimises the field of view, following the setup of de Vries et al. (2021), as shown in figure 3.2a.

Both campaigns produced series of overlapping scans of the water surface in the form of camera frames, aligned perpendicular to the ship track as sketched in figure 3.3. The figure displays the setup when UAV and trawls are deployed for scientific purposes, which happened intermittently in the NPM5 campaign. During this campaign, a camera setup replicating the one of Schwendeman and Thomson (2014) is used, whilst the operational campaigns replicate the one of de Vries et al. (2021). Setup details (height, pitch, roll, azimuth and frequency) are displayed in table 3.2b and explained in section 3.3. The camera field of view varies across the campaigns, and so does the sampling frequency (table 3.2b). For both campaigns, the horizon line must lie within the field of view for the Schwendeman and Thomson (2014) rectification method to be applicable and geotagging to be possible. This method relies on trigonometry to obtain the camera orientation from the inclination and height of the horizon line in the frame (Schwendeman and Thomson, 2014). Information on the camera orientation is used for

(a) Ship-Based Camera Set-up: A GoPro® Hero6 Black clamped to the ship starboard and/or port-side railing.

Camera parameter	NPM5	Ops.
Height (m)	10.2	18.3
Pitch (°)	75	70
Roll (°)	0	0
Azimuth (°)	±90	±90
Frequency (Hz)	0.5	0.2

(b) GoPro Camera Settings. Ops. and NPM5 stand for the operational and research dataset, respectively.

Figure 3.2: Specifics and setup of GoPro camera.

the projection of the detected objects on the water surface, hence the geolocation.

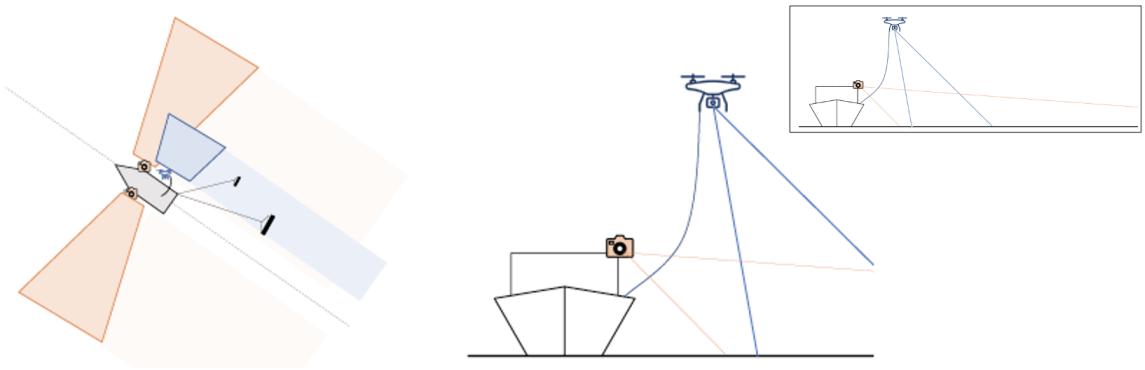

Figure 3.3: Not in scale top and front view simplified sketch of the ship-based camera setup, simultaneous to the UAV and trawl deployment. The camera is clamped to the railing at a height and angle that optimises the field of view to include the horizon line. The field of view of the shipboard camera is more extensive transversal to the ship movement, when compared to the UAV. The opposite applies longitudinal to the ship's movement. The footage of the two devices has an overlapping area.

3.1.1 Ship's wake

A point of concern when measuring velocities around a moving ship is it's wake. The wake is defined as the region of disturbed flow downstream of a solid body moving through a fluid (Colen and Kolomeisky, 2021). It is may be a non-negligible factor affecting surface currents, depending on the position of the camera on the ship, the ship's speed and the distance between the ship's hull and the tracked objects. Computing the wake can help understand a cutoff distance from the ship below which floating plastic's velocities will be influenced. At low speed, the wake can be simplified with a Kelvin wave (Colen and Kolomeisky, 2021). Because of the complexity of the computations and the dependence on the above mentioned factors, accurate

ship's wake computations are omitted from this study. Nonetheless, appropriate checks were conducted before the installation of the cameras by the technicians, imitating Schwendeman and Thomson (2014)'s settings to ensure that the wake effect is negligible when compared to the measurement errors listed in the following sections.

3.2 Supporting data

The ship's displacement and metocean data are logged on shipboard devices and are used for the oceanographic analyses. Measurements' conventions are to be stated clearly in order to avoid confusion, given the different reference frames used in this study, a combination of maritime and scientific conventions. The raw data is collected using the maritime convention of degrees clockwise from North. Overall, directionality is converted from the maritime convention to the vector direction convention of degrees counter-clockwise from East. This is justified by the scientific purpose of this study, as well as to facilitate comparison with oceanographic model results, which are also expressed using this convention.

3.2.1 Ship Motion

In both campaigns, ship motion is recorded at 1 Hz using a Global Positioning System (GPS) for displacement and a Gyro Compass with precision of 0.1° for heading. In maritime terminology, heading is defined as the direction towards which the ship's bow is pointing. This measurement is used when rotating the camera field of view onto geographic coordinates. The rotation is performed using the following rotation matrix:

$$\begin{bmatrix} x_{earth} \\ y_{earth} \\ z_{earth} \end{bmatrix} = \begin{bmatrix} \cos\psi & -\sin\psi & 0 \\ \sin\psi & \cos\psi & 0 \\ 0 & 0 & 1 \end{bmatrix} \begin{bmatrix} x_{ship} \\ y_{ship} \\ z_{ship} \end{bmatrix} \tag{3.1}$$

where ψ is the heading angle. Shipboard GPS is affected by measurement error, which can be in the order of meters (Dalheim and Steen, 2021). In the small scales of this study, this error can be significant and, as previously mentioned, error reduction techniques are applied to reduce the noise as described in later sections.

3.2.2 Sea Surface Current

GPS displacement of a ship is also known in the maritime industry as the speed over ground (SOG), the movement of the ship with respect to the ground. A ship's SOG is influenced by ocean surface currents. In the absence of sea currents, SOG equals the speed through water (STW), the movement of the ship with respect to the water. STW is measured by the Doppler Velocity Log (DVL). The DVL is an acoustic device that uses radio waves betweeen $10^3 - 10^6$ Hz to measure the ship's speed and direction relative to the water (Dalheim and Steen, 2021). It does so by measuring the Doppler frequency shift in a beam of the acoustic wave transmitted from the ship at a depth between 3 and 25 m, depending on the setup. The pulses are reflected by impurities in the water, or density differences (Dalheim and Steen,

2021). A DVL device is present in both NPM5 and operational campaigns. A FURUNO DS-50 was used in the NPM5 campaign and a Skipper DL850 is in use in the operational campaigns. The instruments' standard accuracy is listed in table 3.1.

In an ideal scenario where both GPS and DVL are not affected by measurement error, in 2D, the difference between SOG and STW is the sea surface current. When analysing surface transport mechanisms of passive tracers, this measurement is representative of the total displacement induced by the background flow Laxague et al. (2018). The SOG and STW values consist of a longitudinal and transversal component relative to the ship's heading. The derived surface currents are thus converted to a zonal and meridional component using a trigonometric conversion summarised in the rotation matrix (equation 3.1). The precision of transverse velocity measurements with respect to the ship's movement is generally lower compared to measurements along the ship's track. This is because the instrument's design and signal processing algorithms are primarily focused on the ship's motion in the forward direction (Taudien, 2018). Overall, several recent studies are concerned with the accuracy of DVL measurements (Dalheim and Steen, 2021), particularly on the influence of GPS errors. Peters and Skop (1996) found that GPS errors can lead to pseudo-currents at the submesoscale. Considering the small surface current magnitudes in the study area, these errors can be substantial. However, as above mentioned, filtering techniques are applied to GPS data, which are expected to substantially reduce the influence of measurement error. Furthermore, when the analysis of transport mechanisms is conducted in relative terms, meaning when comparing the objects velocities' to the surrounding water measurements, GPS errors cancel out.

3.2.3 Waves

Alongside a DVL device, a shipboard X-band radar is active during the operational campaigns. Navigational X-band radar is a remote sensing measurement device in the microwave band that can be used to obtain sea state parameters. A Furuno X Band FAR2117 at height of 16.2 m is used to measure wave parameters in the operational campaigns. For wind speeds greater than 3 m/s, the radar is able to detect a part of the incidence radar beams from the reflection on the rough water surface within a 5 km range. The Doppler shift of the returning signal is processed to obtain information on wave height, wave length, wave period, similarly to ground-based measurements (Alpers et al., 1981). These measurements have high temporal (1 Hz) and spatial resolution (5 m).

Although the full ocean wave spectrum cannot be recovered from radar images, in many cases where the wave spectrum is relatively narrow (hence, not applicable to mixed wave regimes), the dominant wavelength and direction can be retrieved from the image using a non-linear mapping transfer function (Alpers et al., 1981). Radar image sequences are first transformed into a function of wave number and frequency using a discrete Fourier transform (Alpers et al., 1981); then, into an energy density spectrum of ocean surface waves using the dispersion relation of water waves. Peak wave period and direction are derived from the frequency spectrum and peak wave length is derived using the dispersion relation once the peak wave period is known. Further details on the operating principles behind such techniques

are described in (Huang et al., 2017).

Wave measurements are relevant for the analysis of transport mechanisms in chapter 4, as well as for an assessment of the geotagging precision as explained in section 3.3. Therefore, WaveWatch III hindcast (Tolman, 2009) at 3 hour and 1/2° resolution is integrated to the NPM5 dataset, as no X-band radar was mounted on the ship. The additional source of error from the lack of more accurate measurements is discussed in chapter 5, although this dataset is not relevant for the analysis on transport mechanisms.

3.2.4 Wind

Wind speed and direction are measured during the operational campaigns using a GILL WindObserver II, robust ultrasonic anemometers at height of 19.4 m. Quality control and filtering techniques have been applied to correct for the ship's motion and to remove outliers. Measurements precision and accuracy are stated in table 3.1. The processed data were averaged to 1 Hz. In practice, anemometers measure the vector sum of the true wind and the wind induced by the motion of the instrument (Reinsvold, 2013). To ensure accurate wind measurements, it is necessary to smooth the data over several wave periods. To do this, the wind measurements taken during the tracking period of detected objects are averaged using a median value.

For comparability with meteorological data, the given wind velocity data is converted in this study to 10 m height using the logarithmic wind profile law (Tennekes, 1973). It is a semi-empirical function commonly used to replicate the vertical distribution of horizontal mean wind speeds within the lower section of the boundary layer. The law is preferred to the wind profile power law in this case, as it is considered to be a more reliable estimator of mean wind speed in the lowest 10-20 m of the boundary layer (Emeis and Turk, 2007). The logarithmic wind profile law is reported as follows:

$$\mathbf{u}(z) = \frac{\mathbf{u}_*}{k} \ln \frac{z}{z_0} \tag{3.2}$$

where $\mathbf{u}(z)$ is the wind vector at height z, $\mathbf{u}_*$ is the shear velocity, an expression of shear stress in velocity units, k is the von Kármán constant (≈ 0.4) and z_0 is the surface roughness length. For a known wind speed at a given height, the formula is rewritten as follows:

$$\mathbf{u_{10}} = \mathbf{u_{20}} \frac{\ln(\frac{10}{z_0})}{\ln(\frac{20}{z_0})} \tag{3.3}$$

where $\mathbf{u}_{10}$ is the wind vector at 10 m height and $\mathbf{u}_{20}$ is the anemometer wind vector at ≈ 20 m height. The surface roughness length is assumed constant in varying sea states for simplicity and it is set to 0.0002 m, which is the value for open sea conditions (Tennekes, 1973).

Lastly, satellite wind observations are integrated in the analysis in chapter 4 for an under-

Table 3.1: Measurements' details for both campaigns. Information has been extracted from the respective user manuals of the measurement devices for the settings implemented on the ship of relevance. When both error magnitude and % of the signal are given, the highest error should be considered.

Parameter	Range	Accuracy	Resolution
Acoustic Sea Current (NPM5)	-	± 0.05 m/s or 1.0%	0.05 m/s
Acoustic Sea Current	-	± 0.1 m/s or 2.0%	0.05 m/s
Wave Height	0.5-20 m	± 0.5 m or ± 10%	0.1 m
Wave Period	3.5-40 s	± 0.5 s	0.1 s
Wave Direction	0-360°	± 2°	1°
Wind	0-65 m/s	± 2% @12 m/s	0.01 m/s
Wind Direction	0-360°	± 2° @12 m/s	1°

standing of the regional wind dynamics during the months of interest. The product used is the Global Ocean Monthly Mean Sea Surface Wind and Stress from Scatterometer and Model 10-m stress-equivalent at 0.25° x 0.25°.

3.2.5 Temperature and Salinity

Temperature and salinity were measured solely during the NPM5 research campaign. They were retrieved from a thermosalinograph at approximately 3m depth. The data has been synchronised with the ship's signal to obtain location data and water surface density has been computec from the salinity, temperature and pressure data following Roquet et al. (2015)'s approximation. The data has then been smoothed to remove high-frequency noise and variability in the data by customising Barceló-Llul et al. (2021)'s method. Firstly, it was interpolated to a regular distance axis with a resolution of 0.2 km, then a LOESS filter (Jacoby, 2000) with a half-power filter cutoff of 10 km was applied, effectively retaining fronts longer than 4 km (Chelton et al., 2011). Although some small scale information was missed in this step, instrumental noise did not allow less coarse resolution. Finally, large-scale variability was computed by applying a LOESS filter with a cutoff of 200 km to the interpolated data.

In chapter 2 a theoretical justification on the importance of convergence and vorticity for floating material accumulation was given. To obtain two-dimensional information on the surface flow and structures, thermosalinograph data is used alongside daily data from The Operational Mercator global ocean analysis and forecast system at 1/12° (Copernicus Marine Service, 2023). This data is obtained by combining numerical models and data assimilation. Surface density, relative vorticity, Rossby number and divergence are computed using Roquet et al. (2015)'s formula, equation 2.1, 2.2 and 2.3, respectively. Results from the analysis of this data are outlined in section 4.2.

3.2.6 Overlapping UAV footage

In the NPM5 campaign, some sections of the transect, hereafter named *stations*, have overlapping GoPro and UAV footage. UAV footage was shot from an approximate height of 25 m above the water, at a frequency of 0.5 Hz. Flight length varied from less than minutes, to

over an hour and a half, depending on metocean conditions and technical limitations.

3.3 Image processing, detection and projection

Following a description of the cameras setup and the supporting data, this and the following sections outline the workflow presented in figure 3.1 in more detail. As they are collected, all GoPro frames are automatically corrected for distortion by the internal camera software, meaning that step 2 in figure 3.1 is automatised. Image processing, detection and projection are conducted using a customised version of the methodology used in de Vries et al. (2021), summarised in steps 3 and 4 in figure 3.1 and explained in detail as follows.

Firstly, the frames are filtered through an adapted version of YOLO v5, a Convolutional Neural Network backbone to form image features (Ultralytics, n.d.). The algorithm was trained on a curated selection of common floating debris in the GPGP (see de Vries et al. (2021) for more details). The outcome of this filtering step is a database of detected objects' images. The location of these objects within the frame is then projected on a local 2D frame of reference on the sea surface through horizon detection, applying Schwendeman and Thomson (2014)'s method. The horizon line is detected by the algorithm as the line that separates the sky from the sea, as a straight line. As shown in figure 3.4a, horizon detection can be used to derive camera orientation, and so, the projection of the field of view on the sea surface. Schwendeman and Thomson (2014)'s method removes the need for precise image stabilization and rectification, which have previously been necessary steps for successful image projection based on shipboard marine motion sensors information. Bypassing image stabilization and rectification allows for a wider application of shipboard remote sensing techniques when precise ship motion sensors are not available and for sea states that would otherwise be too rough for successful image rectification. The method has been tested by Schwendeman and Thomson (2014) for computing wave breaking statistics, and the limitations have been taken under consideration when applying the method to the present study.

For a chosen area within the field of view, the geographic coordinates projection looks as in figure 3.4b. Following Schwendeman and Thomson (2014)'s approach, the error margin of the projection can be estimated, given camera specifics and, ideally, sea state conditions. The sources of error generate from four independent sources:

- camera pitch and roll from horizon detection imprecision,
- camera height due to sea state conditions,
- ship yaw due to compass instrumental variability,
- ship geolocation due to GPS imprecision.

Time discrepancies between measurements can be an additional source of error. Nonetheless, the direct derivation of camera orientation from horizon detection overcomes this issue. Furthermore, the high measurement frequencies of both compass and GPS, mentioned in section

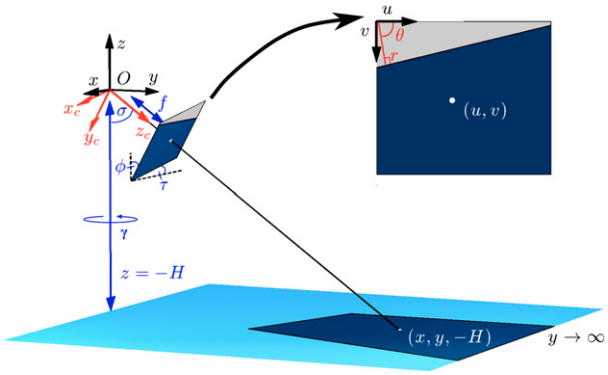

(a) Image to plane projection method defining the camera parameters and coordinate systems from Schwendeman and Thomson (2014). The sea surface is shown in blue, with dark blue corresponding to the camera field of view, while gray areas denote sky. The small rotated square represents the camera sensor (not to scale), and the top-right square shows the resulting image.

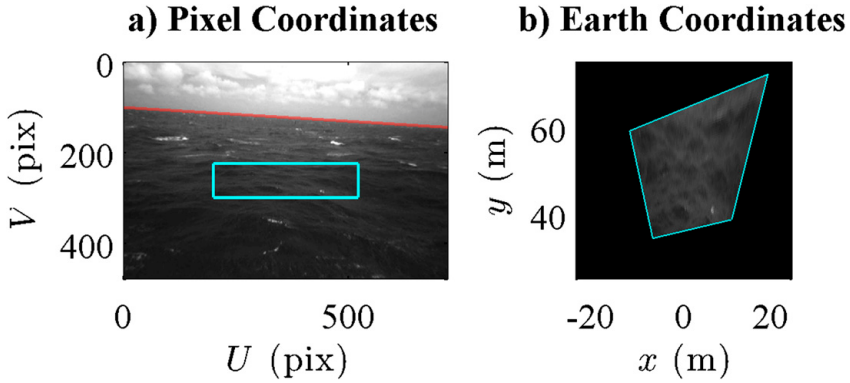

(b) Example of image to plane projection result from Schwendeman and Thomson (2014). (a) The image in pixel coordinates, with horizon detected (red) and a sample rectangle (blue). (b) The projection of the pixels within the blue rectangle to geographic coordinates.

Figure 3.4: Graphical representation of the image to plane projection method. Taken from Schwendeman and Thomson (2014)

3.2, make the time discrepancy-induced error from these devices negligible in comparison to their precision. The listed sources of error can be quantified and aggregated into a Monte Carlo experiment that estimates the variability of the geographic coordinates from the plane projection. This error quantification is an essential component of the velocity estimation method, as it will be used as a filter in section 3.4.1.

Once the objects have been detected and projected in geographical coordinates with respect to the ship, this information is coupled with the ship's GPS position to obtain the absolute geographical coordinates of the objects. The ship's GPS system is used instead of the camera's GPS system, due to the higher precision and frequency of the signal. Once this step is completed, the detected floating plastic contains timestamp information and it is geotagged. Now, object tracking can be performed to compute their displacement over time.

3.4 Floating Debris Tracking

This step (step 5 in figure 3.1) consists in linking the debris between frames, to track the debris displacement over time. The essential part of PTV is to correctly identify and link the same particle in different frames (Malik et al., 1993). In this study, the linking procedure creates one-to-one matching between debris from frame to frame through a remote sensing filtering technique based on the size, colour and displacement of the debris. Certainty of correct detection and linking increases with the number of frames. Longer tracking of an object across the frames reduces the risk of erroneous detections, such as whitecaps, foam, or glare. Hence, a longer observation time allows to filter out the false positives. From testing, on average, the algorithm can be optimized to reduce manual validation, by introducing a minimum linking threshold of 4 frames. This means that a debris item must be detected in at least 5 frames to be considered a valid data-point. Despite the algorithm's good efficiency, some manual filtering has been performed by removing erroneously linked frames and to guarantee a high quality dataset with zero false links tolerance.

Once tracked, the debris displacement is used to derive the velocity. Overall, velocity derivation is influenced by two independent sources of error. Locally, by the precision of the projection to geographic coordinates, quantified in the following section, and globally, by the GPS precision. The latter is a source of error that cannot be easily quantified, as it is dependent on the ship's motion, which is not known with sufficient precision. Therefore, the precision of velocity derivation depends on two factors. First, it degrades locally due to projection errors and second, it degrades globally when GPS precision becomes significant (Malik et al., 1993). Because the two sources of error are independent, they can be quantified separately.

3.4.1 Monte Carlo analysis of PTV

A Monte Carlo method is an often utilised experiment in quantitative sciences that relies on the statistical theory of large numbers (Kwak and Kim, 2017). The theory states that for larger samples, the average of the sample means and standard deviations approach the true population's (Kwak and Kim, 2017). Monte Carlo experimentation is the use of simulated random numbers to estimate the possible outcomes of an uncertain event (Sugita, 2011). For

a large number of simulations, the most likely outcome is approximated by the expected value of simulated samples (equation 3.4), and the same reasoning applies to its standard deviation (equation 3.5).

$$\mathbf{u}_t = E(\hat{\mathbf{u}}_t) = \lim_{N\to\infty} \frac{1}{N} \sum_{j=1}^{N} \hat{\mathbf{u}}_{t,j} \tag{3.4}$$

$$\hat{\sigma}_{\hat{\mathbf{u}}_t} = \sqrt{\lim_{N\to\infty} \frac{1}{N} \sum_{j=1}^{N} (\hat{\mathbf{u}}_{t,j} - \bar{\hat{\mathbf{u}}}_{t,j})^2} \tag{3.5}$$

Here, $\mathbf{u}_t$ is the true velocity (most likely outcome), $\hat{\mathbf{u}}_{t,j}$ is sample j's velocity, $\bar{\hat{\mathbf{u}}}_{t,j}$ is sample j's mean velocity and $\hat{\sigma}_{\hat{\mathbf{u}}_t}$ is its standard deviation. Therefore, a Monte Carlo analysis allows to estimate the accuracy and the variability of the projection to geographic coordinates, subject to the error sources described in section 3.3. When repeated for each frame, the variability of the local velocity estimation is obtained. This variability is an estimate of the error in the local reference frame. The size of the variability is expected to differ based on the location of the object in the camera field of view, in particular its distance from the camera, as the area per pixel ratio increases as the selected pixel is higher in the frame (the pixel covers an area that is further away and hence bigger). Therefore, the precision of the projection in the local frame of reference is studied for the distance bands presented in figure 3.5a. The sea surface section of the field of view is divided for visual representation into three bands representing detections at close, medium and long distance. This separation gives a clear visual separation of the errors' orders of magnitude, proportional to the distance of the point from the camera. Hereby, the results of the Monte Carlo for the NPM5 campaign camera setup are presented, as the results are used in the inter-instrumental validation in a later section (step 9 in figure 3.1). Results from the operational campaign can be found in appendix A. Due to the wider field of view of the operational camera, the variability of the derived velocities is substantially smaller than for the NPM5 camera.

The Monte Carlo experiment consists of the following steps. The variability of the projection is tested for varying values of the sources of error (pitch, roll, heading, height). To do so, a random number generator with a normal distribution (for simplicity) is used for each source of error. A random number generator is a python module that produces a sequence of numbers that meet certain statistical requirements for randomness (Python library, 2023). For each source of error, the instrument's accuracy is used as standard deviation of the random number generator. Because the camera calibration of pitch (σ) and roll (τ) is performed using the horizon line as a point of reference, where θ and r are the relevant parameters visible in figure 3.4a, pitch and roll inaccuracies are solely dependent on the horizon line detection precision (Schwendeman and Thomson, 2014). The inaccuracy of the horizon line detection, hence of θ and r, is based on the camera's pixel resolution, consequently pitch (σ) and roll (τ) inaccuracies are derived from the projection equations (Schwendeman and Thomson, 2014):

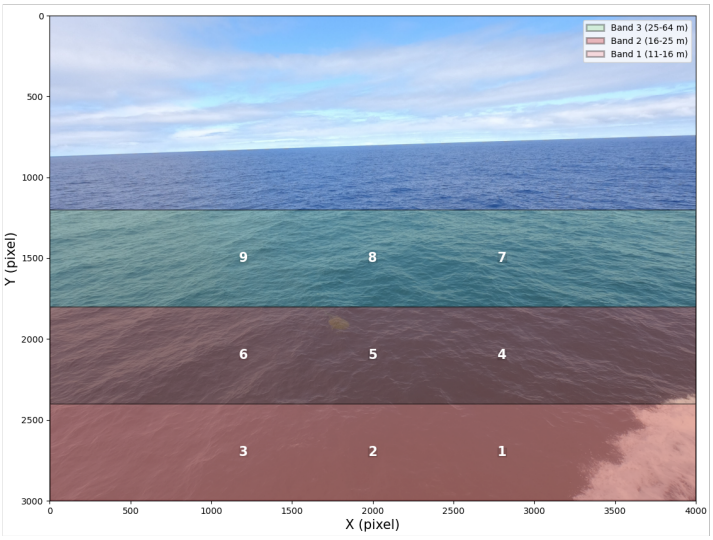

(a) Monte Carlo pixel bands setup. The frame section where most of the debris is spotted is divided in 3 horizontal bands of equal pixel area. The remaining section of sea surface at the distance is ignored in this visual representation, because of the few observations there. On the ocean surface the area per pixel ratio increases as the pixel is higher in the frame. In each band 3 points are annotated along the x axis and projected in figure 3.5b.

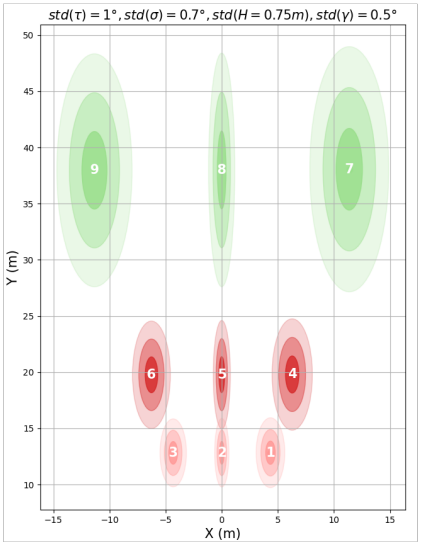

(b) Monte Carlo results of projection variability ($\hat{\sigma}_{\hat{\mathbf{x}}}$) of points on the ocean surface. The plot is colour coded to match the bands in figure 3.5a (e.g. green corresponds to band 3). The x and y coordinates are the projection of the annotated points in the frame on the ocean surface. The shadowed area represents the variability of the projection due to projection error. From darker to lighter, +/- 1, 2 and 3 standard deviations. Errors grow as the point is further away from the camera.

Figure 3.5: Graphical representation of the Monte Carlo analysis.

$$\begin{aligned}\tau &= \tan^{-1}\left[\frac{-f_u}{f_v \tan(\theta)}\right] \\ \sigma &= \tan^{-1}\left[\frac{f_u \sin(\tau)\cos(\theta) - f_v \cos(\tau)\sin(\theta)}{r - c_u \cos(\theta) - c_v \sin(\theta)}\right]\end{aligned} \tag{3.6}$$

where r and θ are the horizon line vector magnitude and angle as displayed in 3.4a, f_u and f_v are the focal length per pixel width and height and, c_u and c_v are the image column and row center, respectively.

Additionally, the projection's imprecision is almost entirely dependent on the wave height due to the dependence of the projection on the z coordinate (Schwendeman and Thomson, 2014) (figure 3.4a). In particular, on the sea height difference between the location of the floating spotted debris and the camera, which is a function of wave height (trough to crest). Hence, significant wave height is taken as an input source of error for the camera height. This very conservative assumption simulates a worst case scenario where the debris and the camera are located at the two extremes of the wave, i.e. $|Z_{\text{camera}} - Z_{\text{debris}}| = 2\sigma(H)$, where $2\sigma(H)$ is the significant wave height (SWH), defined as the mean wave height of the highest third of the waves. Due to the lack of X-band radar measurements in the NPM5 campaign, $2\sigma(H)$ is obtained from WaveWatch III interpolated to the nearest location to the ship. These values are validated with the measurements manually logged during the campaign. $2\sigma(H) = 1.5$ m is taken as a representative value for the NPM5 campaign. Finally, the potential inaccuracy of the compass is taken conservatively as $\sigma(\gamma) = 0.5°$, where γ is the heading and the compass's precision is $0.1°$ (table 3.1.

Overall, the inputs of the Monte Carlo experiment are $\sigma(\tau) = 1°$, $\sigma(\sigma) = 0.7°$, $\sigma(H) = 0.75$ m, $\sigma(\gamma) = 0.5°$. The results are presented in figure 3.5b. The variability is proportional to the distance of the point from the camera, as expected. The variability is substantially smaller longitudinally to the camera's displacement than transversally due to the decreasing pixel to area ratio in the transversal direction. The variability is also smaller in the longitudinal direction due to the lower sensitivity of the projection to the camera's height.

3.4.2 Floating Debris Linearised PTV and Filtering

In this section, results from figure 3.5b are used to filter the data-points that are too noisy (step 8 in figure 3.1). In general PTV theory, the velocity of a point in the flow is estimated by using the fundamental definition of velocity as the time derivative of the position of the particle, namely,

$$v = \lim_{\delta t \to 0} \frac{dx}{d(\delta t)} \tag{3.7}$$

where δx is the displacement of the particle in the time interval δt (Malik et al., 1993). However, due to the nature of the data, δt is small, but not infinitesimal. From the Monte

Carlo analysis, the variability of the projection is proportional to the distance of the point from the camera, however, the velocity precision is also dependent on the length of observation time. Hence, the precision of the velocity is expected to be a function of the distance of the point from the camera and the length of observation time. Furthermore, due to wave motion, the error signal is expected to be periodic and correlated with the wave motion. There are various methods to capture the periodicity of the error signal, such as Fourier analysis. Nonetheless, the periodicity of the signal is not necessarily constant and complexly linked to the wave frequency spectrum and other sources of error. Therefore, such methods are not applied here, and instead, given the short tracking time window, object displacement is linearised. The linearisation consists of the derivation of a point velocity per object, obtained from performing a linear regression on the object's displacement over time. Mathematically, this step is described in equation 3.8:

$$d\mathbf{x}_t = \mathbf{x}_t - \mathbf{x}_0 \approx \beta_0 + \beta_1 t + \epsilon \tag{3.8}$$

where, $\mathbf{u}_t \approx \beta_1$.

The linearisation is a compromise between having sufficiently precise velocity measurements, and reducing the error signal. This simplification implies that small scale features are neglected and assumed constant over the time window of detection (which often lasts less 1 minute). Due to the substantial difference in error size longitudinal and transversal to the ship's direction, the linear regression is performed separately on the two components. The absolute displacement and direction are then obtained as the magnitude and vectorisation of the longitudinal and transversal components.

Once the linearisation is performed, an estimate of the margin of error in the velocity derivation is obtained using the Monte Carlo analysis results from section 3.4.1. This error estimation is a valuable information to understand the signal to noise ratio and apply adequate filtering techniques. The procedure consists of the following, and it is a replica of the projection Monte Carlo experiment, now repeated on the velocity computations.

For all lengths of tracking time and positions in the frame, the linearised trajectory is added a stochastic noise signal, with standard deviation obtained from the Monte Carlo projection (figure 3.5b). This noise signal is added to each point in the displacement at the same frequency as the camera's footage rate (see table 3.3), to emulate the projection error. The standard deviation of the simulated samples (equation 3.4) is obtained by repeating this experiment for a large number of simulations. For each measurement, based on the wave conditions, length of tracking time and distance from the camera, a value is obtained and displayed in figure 3.6. This value is used to filter derived velocities that are too noisy. As a minimum requirement, all the velocities with a standard deviation that is greater than $\hat{\sigma}_{\hat{\mathbf{u}}} = 0.1$ m/s are discarded. This choice comes from trial and error and it is a compromise between the need to filter out noisy data and the need to retain as much data as possible for a statistically significant study. Hence, it is a threshold that is applicable to this particular dataset, and may differ in other scenarios. Ideally, the threshold would have been set to

$\hat{\sigma}_{\hat{\mathbf{u}}} = 0.05$ m/s. Hence, all values that are above the line $\sigma = 0.05$ m/s in figure 3.6. This filter would guarantee, based on a normal distribution, that around 66% of the derived velocities are within the margin of error of $\pm\hat{\sigma}_{\hat{\mathbf{u}}} = 0.05$ m/s. In practice, however, this would result in the loss of a substantial amount of data. Furthermore, the Monte Carlo analysis is conducted taking input error values from the worst case scenario, namely, the error is taken from the scenario where the item and the camera are at the antipodes of the wave motion.

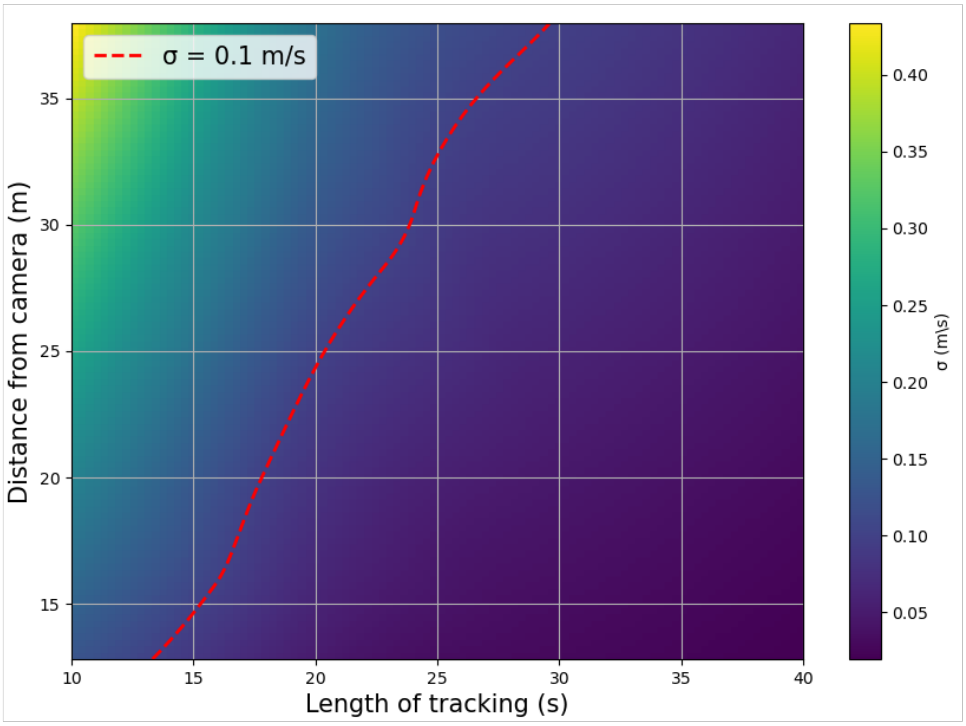

Figure 3.6: $\hat{\sigma}_{\hat{\mathbf{u}}}$ is the expected value of the standard deviation of the measured velocity, obtained from the Monte Carlo experiment. The red line represents the filter cutoff value applied to the derived velocities. This plot is derived from the inputs of figure 3.5b on NPM5 data.

Whilst this is a sufficient approach for the analysis of the transport of floating debris in the local frame of reference, as previously mentioned, an error source that has been left out of the Monte Carlo analysis. This is the GPS signal error. Despite the high precision of the ship's GPS signal, the error can be significant when considering small displacements. When the ship's heading is constant, linearisation of the GPS track during the tracking time of each object is performed to reduce the typical variability of GPS signal (Dalheim and Steen, 2021). This is a method that is often used in spatial sciences (Blewitt, 1997). This linear displacement is then added to the object's relative displacement to obtain the object's total displacement, expressed in geographic coordinates.

3.5 UAV and GoPro PTV comparison

Areas of overlapping UAV footage are used as a secondary measurement, for comparability with the GoPro-derived velocities and as a validation step of the above described methodology (step 9 in figure 3.1), before implementation on the larger operational dataset. This inter-measurement comparison is the most robust validation method available in this study, to quantify the precision of the method. In theory, UAV-derived velocities should have higher precision, due to the more precise geotagging of the items, given its verticality. Ideally, validation would entail a one to one comparison of the object's position in the UAV and the GoPro footage. However, due to the different camera angles, tracking single matching objects was only possible for too few items to draw statistically significant conclusions. Instead, the comparison is performed at a station level, through the use of spatial clustering techniques. Clustering is performed by defining a spatial box around each UAV strip of images so that all objects detected by the two measuring devices are included in it. Each station is approximately 0.2° by 0.2° in longitude and latitude. A visual representation of the overlapping boxes is presented in figure 3.7a. Each station's name is taken from the original research campaign's design. Missing stations are areas where at least one measurement device did not spot any debris. Assuming that samples of detected debris are comparable across measurement device, transport can also be compared. An important consideration is that the number of items detected in the same box is not necessarily the same for the two measuring devices. This is due to the different camera angles and the different detection capabilities (refer back to figure 3.3). Nonetheless, the scope of the comparison is to get an approximate order of magnitude of the accuracy of the GoPro-derived velocities for implementation of the method on the operational dataset. Hence, the number of items detected in the box is ignored in this statistical comparison.

Each measurement's device cluster statistics are computed as follows:

$$\mathbf{v}_{\text{station}}(\mathbf{x}, t) = \frac{\sum_{i}^{S} w_i \mathbf{v}_i(\mathbf{x}, t)}{S} \tag{3.9}$$

where $\mathbf{v}_i(\mathbf{x}, t)$ is the single object's velocity, w_i is its given weight and S is the number of items in the station for each measurement device. The weights, denoted as w_i, are assigned to each observation based on its reliability. These weights are based on the inverse of the variance, i.e., $w_i = \frac{1}{{\sigma_i}^2}$, where σ_i is the standard deviation of the i-th observation. Hence, the higher the standard deviation, the lower the weight assigned to the data point. Here, the standard deviation of the observations is obtained from the Monte Carlo results for the GoPro. Weights are assigned to the UAV observations based on the duration of the tracking instead. The differentiation in the filtering between UAV and GoPro velocities relies on the assumption that UAV geotagging is closer to the ground truth, so that a Monte Carlo analysis was not conducted. Additionally, each item i is subject to conditions $i = [i|T_i > 10 \text{ s}]$ for UAV, and

$i = [i|\sigma(\mathbf{v}_i(\mathbf{x}, t)) < 0.1$ m/s] for GoPro, to filter noisy data-points. Finally, $\mathbf{v}_{\text{station}}(\mathbf{x}, t)$ is the weighted average for each measurement device in each station, displayed in figure 3.7b.The methodology is defined sufficiently accurate if in each station, velocities across measurement devices lie within the chosen error threshold of 0.1 m/s (recall from section 3.4.1) from each other (figure 3.7b). Nonetheless, it should be kept in consideration that the detected debris may be different across the two measurement devices.

Figure 3.7b clearly displays a variability of transport across stations. Furthermore, there is some clear variability within station (at the mesoscale and smaller). Overall, the performance of the GoPro-derived velocities seems satisfactory, given the small sample size, with station-wide velocities within less than 0.1 m/s across measurement device, except for station H and I. There, the discrepancy in the derived velocities could be caused by difference in spotted items across measurement device. Finally, given the lack of additional validation data, the methodology is applied on the wider operational dataset, whilst remaining aware of the limitations showed in both section 3.4.1 and here.

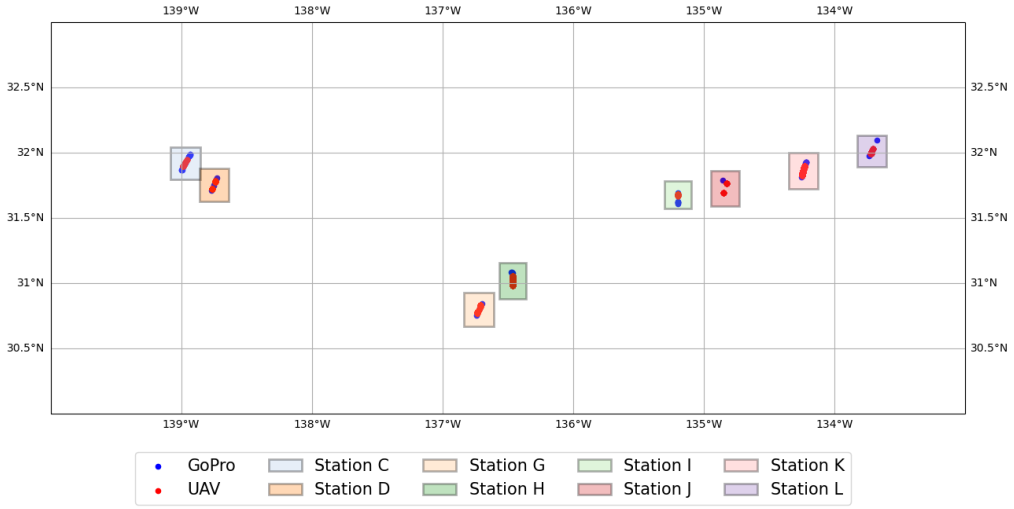

(a) Map of stations with overlapping UAV and GoPro footage. Boxes represent the stations' area of analysis and the dots are the object detections from each measurement device.

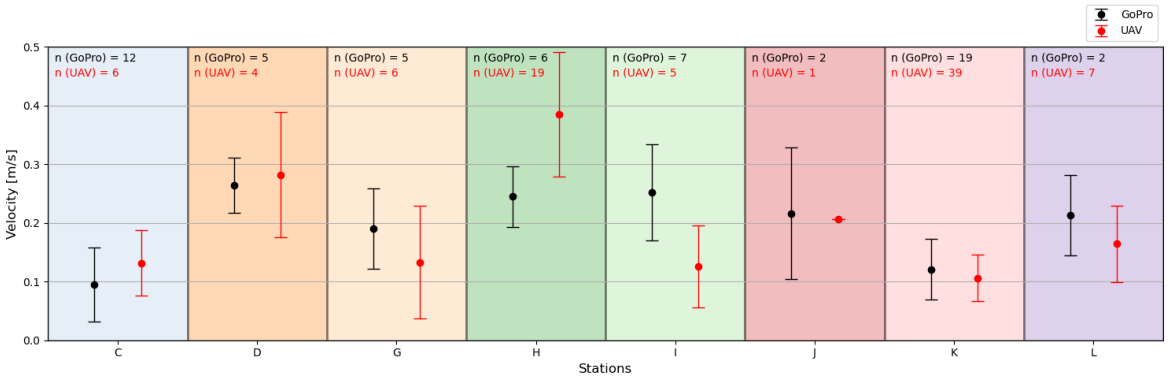

(b) Comparison of UAV- and GoPro-derived velocities in each station. In red the UAV-derived velocities and in black the GoPro's. Points represent the weighted mean velocity and the bars represent the standard deviation. In station J no standard deviation is displayed for UAV given the sample size of 1.

Figure 3.7: UAV stations and inter-measurement velocity comparison.

Chapter 4

Results

This chapter is divided into two main sections. Firstly, an analysis of the transport mechanisms of measured floating plastic displacement is conducted on the operational dataset, where in situ metocean data is collected (see chap 3). Secondly, the spatial distribution of floating plastic at meso- and submesoscale is investigated by analysing the NPM5 thermosalinograph and floating plastic detections data.

4.1 Transport mechanisms

Results in this section investigate the dominant transport mechanisms of floating plastic in the North Pacific Subtropical Gyre through the application of the previously presented methodology on an in situ dataset gathered from extensive presence in the GPGP. In order to adequately analyse measured transport of floating plastic, it is crucial to first understand the spatio-temporal distribution of the observations, so that a correct analysis framework can be built. Indeed, transport mechanisms' importance is both time and space dependent (see chapter 2 and figure 2.1). Hence, information on how long floating plastic is tracked for and how far it displaces is presented in figure 4.1. Given the dataset's spatial distribution, the focus of this study is on the North-East region of the North Pacific Subtropical Gyre, as all observations lie within (31-39°N,138-143°W). For spatial context, observations are plotted on a time-averaged model predicted floating plastic mass concentration isoline from Lebreton et al. (2018) between the time of the first and last observation. The isoline is defined as where the mass concentration is twofold the average mass concentration of the entire model grid (refer to Lebreton et al. (2018) for further details on the model outputs). Most floating plastic is tracked between August and November 2022, with observations in October making up over a third of the dataset. This is the result of several factors, both physical and operational. Spatial heterogeneity is likely the most relevant physical factor. Nonetheless, further investigation needs to be conducted on whether areas of higher concentration were crossed during these months, as the filters applied for accurate velocity measurements have an impact on the true distribution. Indeed, the filtering applied in section 3.4.1 is dependent on tracking

time, distance from the camera and wave conditions, which are not randomly distributed in space. Furthermore, operational factors such as the total area covered and the duration of the campaign have an impact on the distribution over time. Hence, this dataset is not appropriate for density studies. Furthermore, floating plastic's trajectories are mostly shorter than 20 meters, as most observations are shorter than a minute long. Nonetheless, some items are observed for over 4 minutes and displace more than 120 meters. These observations have occurred during periods of time when the ship was stationary. Furthermore, the median size of detected items was a_{min}= 0.4 m (minor axis, recall chapter 1), with a narrow distribution and standard deviation of 0.2 m. Because larger samples are more representative of the true population (Kwak and Kim, 2017), only the months with the most numerous samples are considered for the temporal analysis. This is from August to November 2022.

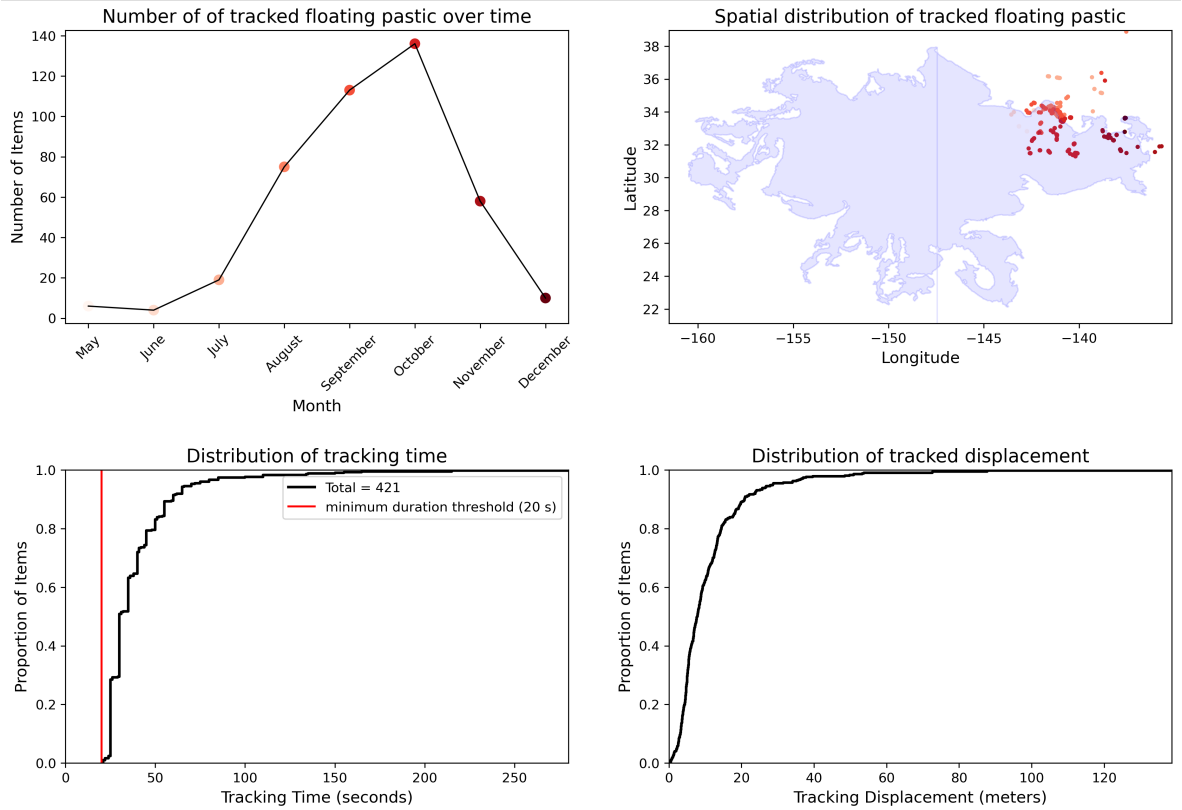

Figure 4.1: a) Distribution of tracked plastic across time that compose the dataset of interest. b) Spatial distribution of tracked floating plastic, focused on the North-West region of the GPGP. Observations are superimposed a time-averaged isoline, where the mass concentration is twofold the average mass concentration of the entire model grid between the time of the first and last observation taken from Lebreton et al. (2018). c-d) Distribution of tracking time and displacement.

4.1.1 Surface current-driven transport

Figure 4.2 is a graphical representation of the velocity vectors of all tracked floating plastic that meets the filtering requirements for this analysis. This plot displays how, within subtropical gyres, surface currents are often weak, below 0.5 m/s. This is consistent with what expected based on Ekman theory, as wind forcing is weaker inside the gyre. Large scale dynamics appear evident and prevailing in the observations from August and October, with the majority of transport uniformly displacing items anticyclonically, driven by Ekman plus geostrophic currents. Large-scale dynamics appear less evident in the observations of October and November, potentially due to the more central location in the gyre. There, a substantial reduction in the average transport strength is evident, when compared to the previous period. Some small scale rotational structures resembling eddies can be spotted in the month of October in the southern region of the plot, with (32.5°N, 141°E) being the most prominent. Finally, when overlapping with wind data, it is evident that in the stronger transport scenarios, wind is influencing both the magnitude and the deflection of the trajectory with respect to the local prevailing surface currents. This hypothesis is investigated further in the next section.

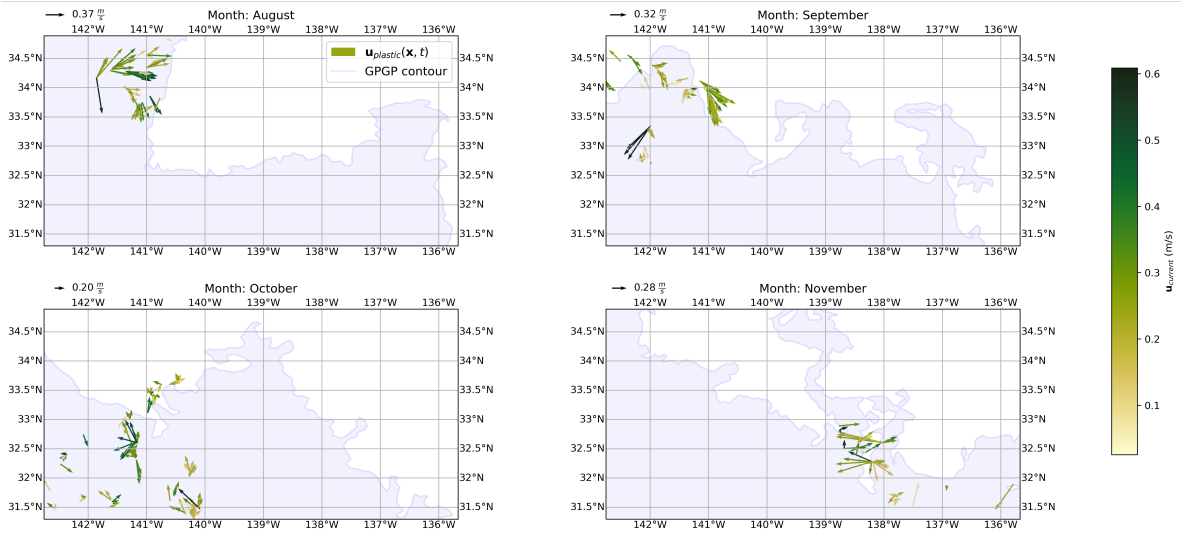

Figure 4.2: Monthly distribution of tracked floating plastic velocities over-imposed on mass concentration isolines defined in figure 4.1. The quiver lengths are proportional to plastic velocities and each subplot's legend displays the average velocity in that month. The quiver color mapping corresponds to the measured sea surface current velocities from the DVL at the time of the observation.

Based on the general consensus in the literature (Lebreton et al., 2018; 2022; Ruiz et al., 2022) that floating plastic accumulating in the North Pacific Subtropical Gyre are heavier floating objects, subject to low to null direct wind drag, a linear relationship between measured plastic velocities and surface current velocities should be able to explain the general dynamics in the region. In this study such assumption is, however, an over-simplification, as detected items in the sample could include objects that are travelling through the gyre and that are not trapped

there. Nonetheless, assuming that such items make up a small percentage of the tracked plastic and that the assumption of dominant current-driven transport is indeed accurate, the linear fit should be representative of most of the measured velocities. The top-right subplot of figure 4.3 displays the described fit, a weighted least squares method. A weighted least squares (WLS) method is a linear least squares method used for the estimation of unknown parameters in a linear regression model, in which knowledge of observational error is taken into account (Cohen and Migliorati, 2016). To fit a weighted linear regression model, the goal is to minimize the weighted sum of squared residuals, to find the optimal values for the parameter vector β as follows:

$$\arg\min_{\beta} \sum_{i=1}^{n} w_i \left| y_i - \sum_{j=1}^{m} X_{ij}\beta_j \right|^2 = \arg\min_{\beta} \left\| W^{\frac{1}{2}}(\mathbf{y} - X\boldsymbol{\beta}) \right\|^2 \tag{4.1}$$

The function is expressed in summation notation on the left, where n is the total number of observations, $w_i > 0$, y_i and X_{ij} are the weight of the i^{th} observation, the dependent and the independent variables, respectively. Additionally, m represents the number of features. On the right, the same formula is expressed in vector notation. When a constrained, single explanatory variable linear regression is applied, $m = 1$.

In this analysis, the linear regression is applied to the speed, neglecting directionality, to first compare the magnitudes. Assuming that displacement is only surface current-driven, linearity should hold. The underlying, single feature equation, is:

$$\mathbf{u}(\mathbf{x}, t) = \beta_0 \mathbf{u}_c(\mathbf{x}, t) + \epsilon \tag{4.2}$$

where β_0 is assumed to be unity and $E(\epsilon) = 0$. Because this relationship is assumed from physical knowledge, this method is called a physics-informed linear regression (Bünning et al., 2022). The linear regression is constrained, meaning that it is forced through the intercept. This makes physical sense in a non-inertial, current-driven setup, as the objects are expected to remain at rest when the ambient water is still. The results of the linear regressions in this study, including slope estimation, wellness of fit and error follow Neter et al. (1996). Excluding the influence of measurement errors, which have been limited through the Monte Carlo filtering, the distribution of the data points in the top-left corner of figure 4.3 indicates non-linearity. The data appears to split in two main clusters, floating plastic speed is mostly weaker than sea surface current in the lower end of the spectrum, and vice-versa at the top. Furthermore, β_0 is larger than unity, potentially due to the higher magnitude outliers. This behaviour could be fully justified by the role of an additional forcing such as upwind and downwind motion, for items that have wind-dependence.

The box-plot on the top-right corner of figure 4.3 displays the distributions of surface current and plastic velocities. The median of both values is highly comparable, suggesting that surface currents are a good explanatory variable of overall transport of floating plastic in the

region, in median terms. Nonetheless, the more pronounced positive tail in the distribution of the velocity of plastic and the poor linear fit performance, suggest that there could be other explanatory variables in place and that there is a clear transport heterogeneity. Based on the fluid mechanics theory described in chapter 2, heterogeneity in transport for fixed forces could be justified by the role of object characteristics, such as shape, size and density. Assuming that the wind could be an explanatory variable, the more extreme plastic velocities could be justified by additional wind-induced drift. This is mainly the wind-drag component of the leeway acting on the buoyant section of the objects, as consistent with what is seen in the field and the literature (Breivik et al., 2011; Maximenko et al., 2018; Quoc et al., 2013). Wind-drag is, of course, also effective in reducing transport speed when working in the opposite direction of surface currents, and this could likely explain the measured floating plastic velocities clustered below the regression line. This is a valid assumption, as the higher floating plastic velocities are not matched by the surface currents in the top-right subplot and are likely caused by a mix of three main components: leeway, inertia and measurement error. A robust assessment of the role of inertia would require measurements of the forces that acted on the object prior to the tracked displacement, which in this case are not available. Chapter 5 describes this limitation. Additionally, figure 4.3 displays a substantial variability in $\mathbf{u}_{plastic}$, within the small region, spanning 0-0.9 m/s. There is also an evident temporal variability in the velocities of both surface currents and, consequently, plastic. These however, have also spatial dependence. Spatio-temporal surface current variability will not be the focus of this section, although it deserves further investigation.

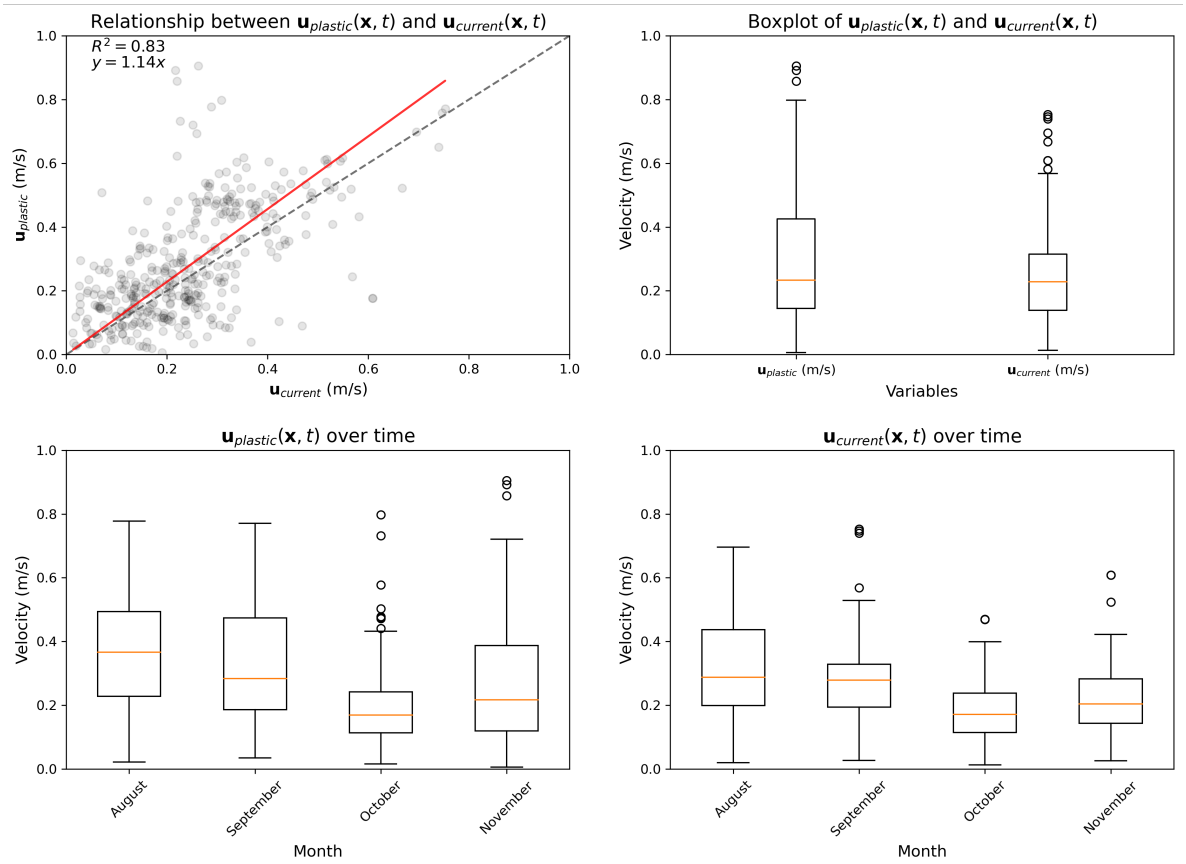

Figure 4.3: a) Relationship between plastic transport and surface currents. b) Statistical visualisation of the distribution of the sample plastic transport and surface currents. c-d) Statistical visualisation of the distribution of the sample plastic transport and surface currents over time to investigate temporal variation and seasonality.

4.1.2 Leeway

The role of leeway is investigated further based on the discussion in section 4.1.1. In chapter 2, leeway is described as an additional transport mechanism that is independent of sea current-induced transport. Therefore, the role of leeway can be investigated by studying the variability of the residuals:

$$L_r \mathbf{u}_w(\mathbf{x}, t) = \mathbf{u}(\mathbf{x}, t) - \mathbf{u}_c(\mathbf{x}, t) \tag{4.3}$$

where, in this case L_r is the leeway rate (from equation 2.9). From now on, the velocity residual $L_r \mathbf{u}_w(\mathbf{x}, t)$ is referred as leeway vector, following Quoc et al. (2013)'s approach.

In order to investigate the role of leeway, an analysis on regional wind conditions needs to be conducted. From figure 4.4, mesoscale wind forcing in the study region is observed to be small, hardly reaching values higher than 5 m/s. These values are substantially smaller than the forcing in the southern region of the gyre, where the strong prevailing winds induce the convergence.

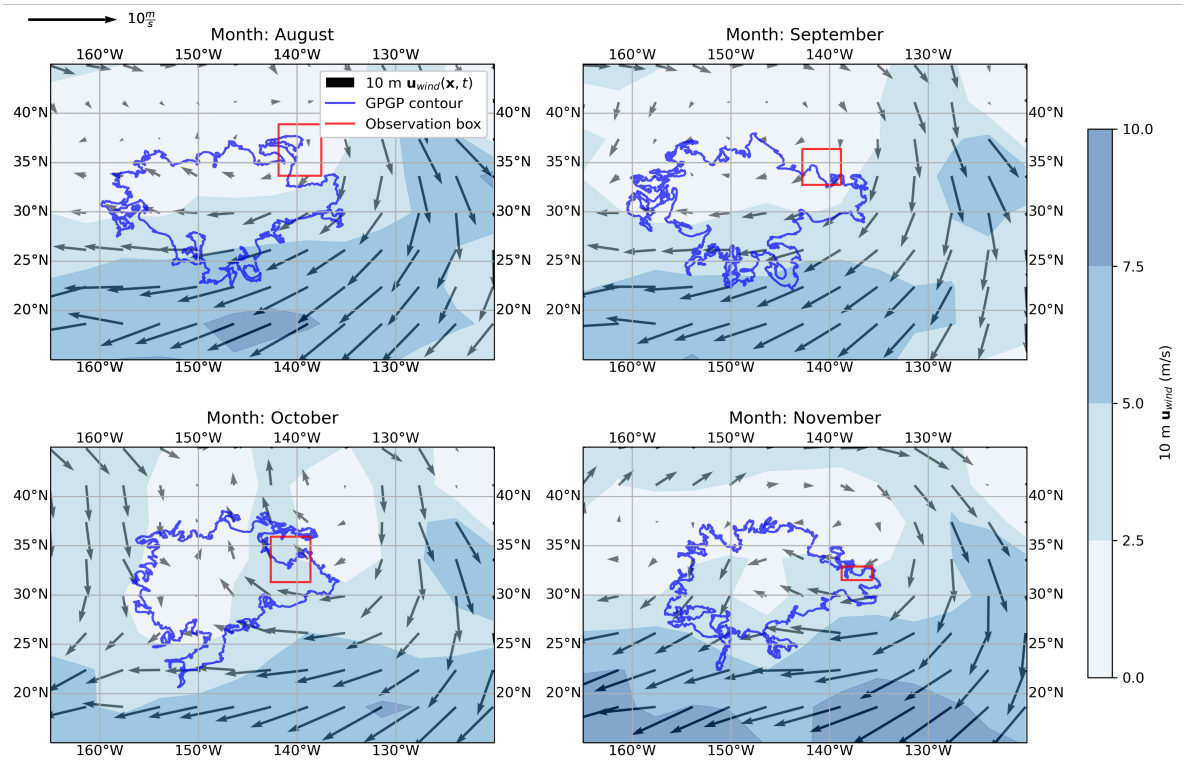

Figure 4.4: Monthly averaged 10 meter wind velocity field from Copernicus scatterometer product described in section 3.2, with superimposed mass concentration isolines defined in figure 4.1 and domain box of tracked floating plastic.

In chapter 3 a maximum threshold of measurement variability is set at $\pm$ 0.1 m/s. Hence, only a leeway signal above $\pm$0.1 m/s is defined statistically significant. Therefore, to ensure that measurement error does not result in fictitious transport phenomena and to avoid wind direction fluctuations at low speeds, mentioned in section 3.2, leeway is analysed only for ship-based measured wind strengths where the signal to noise ratio is sufficient. Therefore, the data can be split between *low* and *high* wind regimes, with a splitting threshold of 5 m/s wind speed at 10 meters. In figure 4.4, on average, magnitudes are lower than the threshold. However, more localised wind phenomena, detected from the ship-based anemometer and described in section 3.2, allow 5 m/s minimum wind speed filtering, guaranteeing a sufficient sample size. This division is justified by the linear fit applied to the downwind transport component, displayed in table 4.1. There is a clear improvement in the explanatory power of the linear fit in low wind regimes, when compared to the whole dataset, suggesting that the

leeway signal may be negligible at such wind strengths. Furthermore, $\beta_0 < 1$ in all scenarios, possibly due to the fact that there is a deflection angle, L_α, in the drift vector with respect to the wind direction, such that a portion of the signal is transferred to the crosswind component.

Table 4.1: Linear regression of floating plastic transport and surface current for varying wind regimes. All results are reported with two decimal digits.

Equation	**Sample**	R^2	**N**
$\mathbf{u}(\mathbf{x},t) = 0.89\mathbf{u}_c(\mathbf{x},t)$	All wind regimes	0.40	382
$\mathbf{u}(\mathbf{x},t) = 0.70\mathbf{u}_c(\mathbf{x},t)$	High wind regime	0.16	162
$\mathbf{u}(\mathbf{x},t) = 0.95\mathbf{u}_c(\mathbf{x},t)$	Low wind regime	0.56	220

Figure B.1 displays the distribution of cross and downwind leeway and surface current. Leeway variance is substantial, over 1 m/s, although some values may be erroneous. Intuitively, if wind is a relevant transport mechanism, downwind leeway should always be positive, within the margin of error of ± 0.1 m/s. In the top-left corner of figure 4.5, the statistical significance of wind-driven transport is evident by the downwind leeway median being significantly above zero, which is not the case in the crosswind direction. Downwind leeway is overall of higher magnitudes, as expected from similar studies (Allen and Plourde, 1999; Breivik et al., 2011), whilst crosswind leeway is closer to being null overall, with variability that is in theory induced by object characteristics, but also influenced by inertia (Breivik et al., 2011). Items with negative downwind can be assumed to be not wind-driven, with values below -0.1 m/s likely caused by error in surface currents, floating plastic velocity measurements, or inertia. In the bottom-left corner of figure 4.5, downwind currents and plastic transport show non-linearity, due to the leeway-induced heterogeneity in transport in similar background current conditions. In the crosswind component, although showing variance, there is linear behaviour.

Furthermore, leeway deflects floating plastic trajectories with respect to the surrounding background currents. In fact, only 43.5 % of items have an angle of deflection smaller than 30° in high wind regimes (> 5 m/s), compared to 65.9 % in low wind (< 5 m/s).

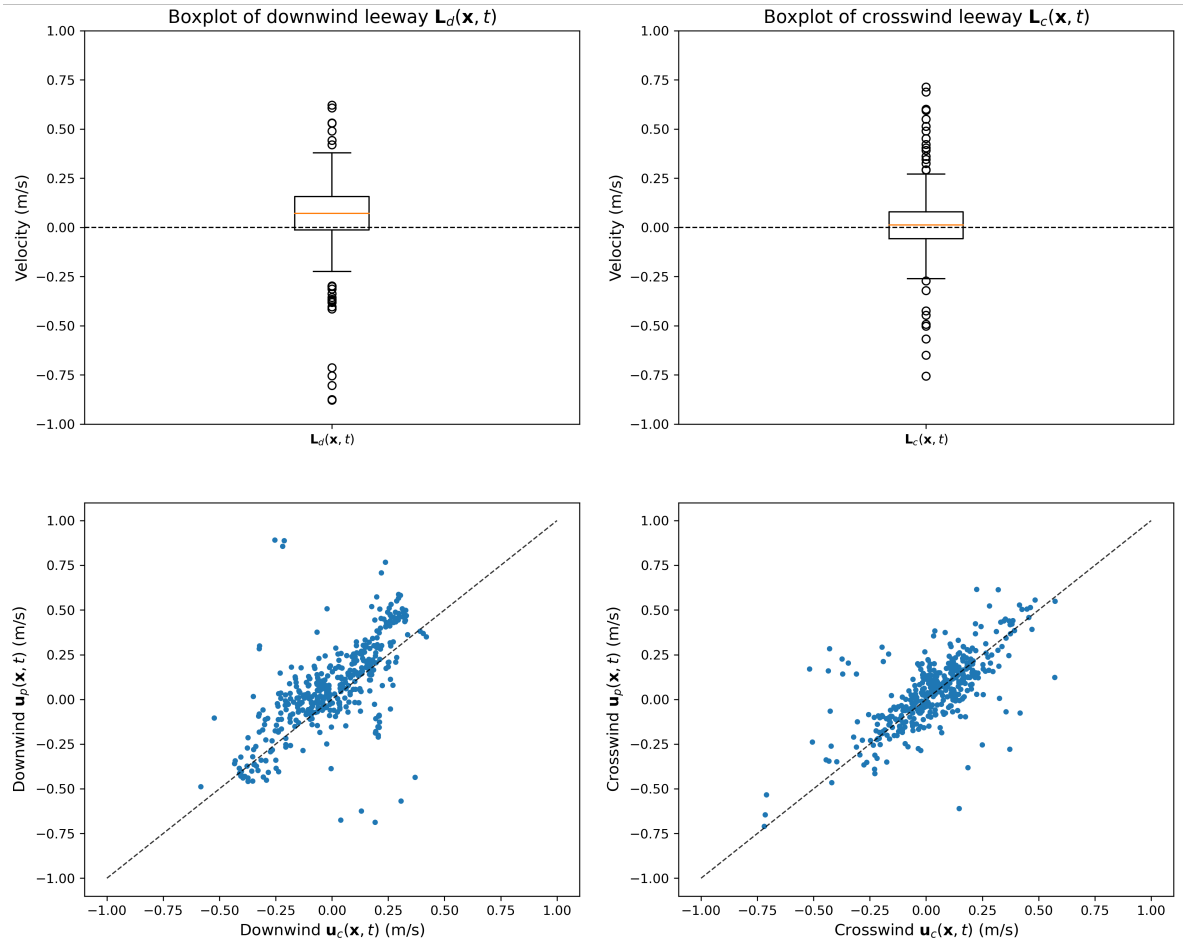

Figure 4.5: a-b) Distribution of cross and downwind leeway as boxplots. c-d¿) Correlation plots between currents and plastic transport in the down- and crosswind directions. The sample's downwind leeway is a positive, statistically significant signal. There is non-linearity in the correlation between downwind current and transport suggesting the influence of wind.

The heterogeneity in leeway magnitudes requires further investigation across time and space, as well as in non-dimensional terms (L_r). This analysis is summarised in figure 4.6. There, the time evolution of the variability in down- and crosswind leeway is compared to the one of the the wind velocity at 10 meters and to, θ, the angle between the surface current and the wind vectors. The bottom row in figure 4.6 are the resulting leeway rates. If all objects behave alike, the variability in the down- and crosswind leeway (top row), should be only determined by the variability in the wind (middle row). Most of the downwind leeway is consistent with the wind forcing (top and middle left), as the wind strength is stronger during the month of August, on average, and weakest in September. Despite the small variation in wind strength and θ, the month of November has the most variant downwind and crosswind leeway, potentially due to differences across objects. Overall, certain periods display more homogeneous leeway rates than others (bottom row), such as August in the crosswind direction and September downwind, compared to October and November, respectively. This observations are quantified below in table 4.2. Finally, these results show evidence of heterogeneity in leeway rates across the sample that deserve further investigation and may hint to differences in dominant transport mechanisms across items.

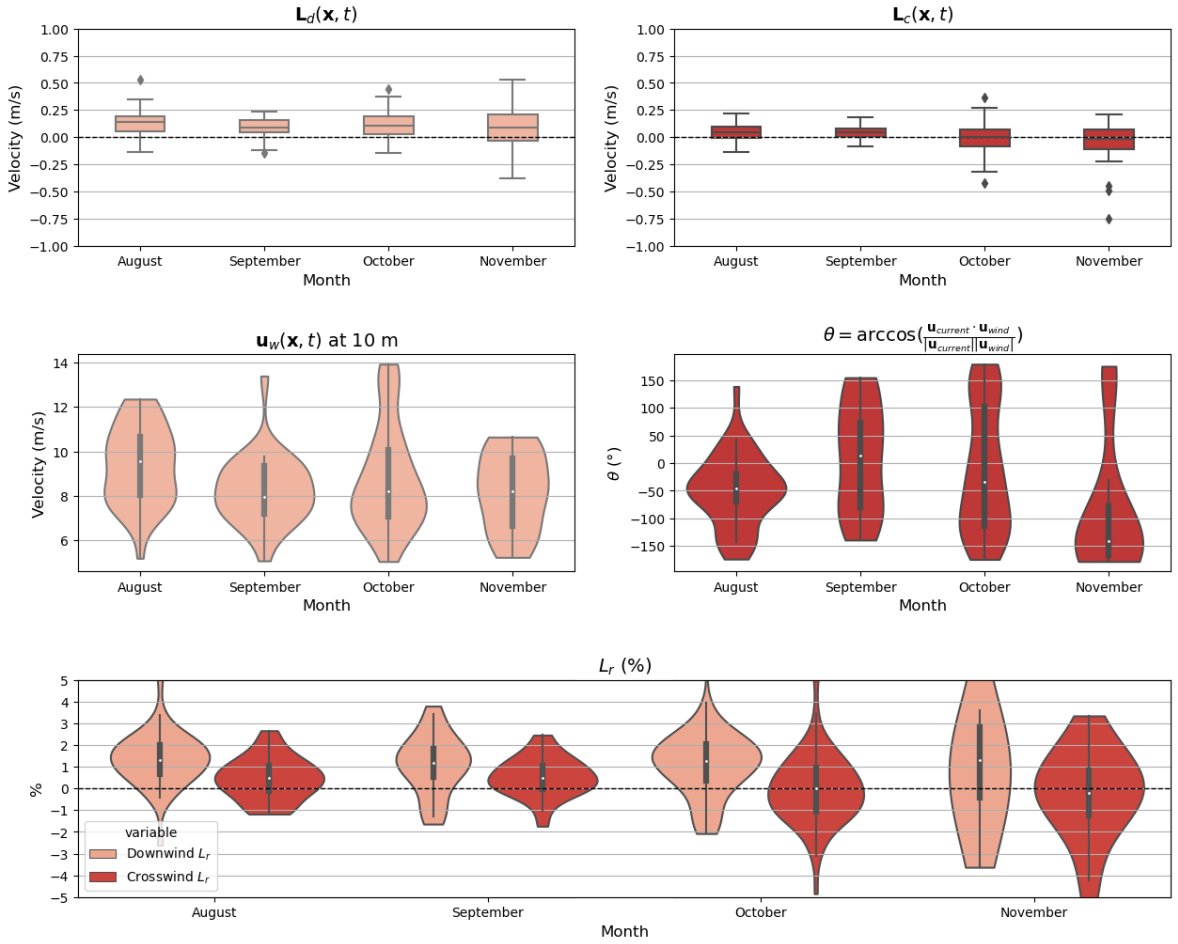

Figure 4.6: Distribution of cross and downwind leeway over time. a-b) The top row are the time evolution of the variability in down- and crosswind leeway. c-d) The middle row are on the left, the time evolution of the the wind velocity at 10 meters and on the right, θ, is the angle between the surface current and the wind vectors. e) The bottom row is the time evolution of down- and crosswind leeway rates.

Due to the linear independence of leeway and current-driven transport, physically-informed multiple linear regression based on equation 2.9 can be applied to replicate the total transport. The formulation is as follows:

$$\mathbf{u}(\mathbf{x}, t) = \beta_0 \mathbf{u}_c(\mathbf{x}, t) + \beta_1 \mathbf{u}_w(\mathbf{x}, t) + \epsilon \tag{4.4}$$

Where β_0, β_1 are the coefficients of interest. This method is adopted in the attempt to explain the non-linearity of the signal in figure 4.3 and 4.5. If the inclusion of a wind component improves the explanatory strength of the fit with statistically significant coefficients β_0 and β_1 (p-value > 0.05), then the presence of leeway can be inferred statistically and its role can be studied in depth. The linear regression equations, wellness of the fit and sample size for

the leeway speed, downwind and crosswind components of leeway are summarised in table 4.2.

Table 4.2: Multiple linear regression results for downwind and crosswind leeway components. Subsets from August and September are analysed for insights on heterogeneity. All results are reported with two decimal digits, based on measurement devices precision (see table 3.1).

Equation	**Sample**	R^2	**N**
$\mathbf{u}(\mathbf{x},t) = 0.70\mathbf{u}_c(\mathbf{x},t)$	Downwind	0.16	162
$\mathbf{u}(\mathbf{x},t) = 0.84\mathbf{u}_c(\mathbf{x},t)$	Crosswind	0.70	162
$\mathbf{u}(\mathbf{x},t) = 1.58\mathbf{u}_c(\mathbf{x},t)$	Downwind (August only)	0.87	38
$\mathbf{u}(\mathbf{x},t) = 0.93\mathbf{u}_c(\mathbf{x},t)$	Crosswind (September only)	0.95	28
$\mathbf{u}(\mathbf{x},t) = 0.63\mathbf{u}_c(\mathbf{x},t) + 0.02\mathbf{u}_w(\mathbf{x},t)$	Downwind	0.44	162
$\mathbf{u}(\mathbf{x},t) = 0.84\mathbf{u}_c(\mathbf{x},t) + 0.00\mathbf{u}_w(\mathbf{x},t)$	Crosswind	0.70	162
$\mathbf{u}(\mathbf{x},t) = 1.25\mathbf{u}_c(\mathbf{x},t) + 0.01\mathbf{u}_w(\mathbf{x},t)$	Downwind (August only)	0.92	38
$\mathbf{u}(\mathbf{x},t) = 0.97\mathbf{u}_c(\mathbf{x},t) + 0.01\mathbf{u}_w(\mathbf{x},t)$	Crosswind (September only)	0.96	28

Overall, fit performance increases when wind-driven transport is added, not surprisingly, with a higher coefficient and better improvement in the downwind direction. Furthermore, all coefficients are statistically significant, except for the crosswind leeway coefficient in September. Nonetheless, the fit performance is still low, especially in the downwind direction, where less than 50% of the variance is explained by the linear fit. The hypothesis that this result may be due to the heterogeneous behaviour across items is confirmed when analysing more localised behaviour, such as taking a section of the data of one specific month. The month of August is the most homogeneous in downwind terms, as showed by the high fit performance. Here, wind clearly plays an important role, given the high leeway and current coefficients (exceeding unity). Crosswind, September is an interesting section, where surface currents explain the almost entirety of plastic transport. Overall, these results, although confirming a wind-dependency in the transport, reject the simplification that the detected items are subject to wind forcing homogeneously. Additionally, the cross and downwind separation has helped clustering different wind behaviour, like suggested in (Allen and Plourde, 1999). Therefore, leeway heterogeneity is investigated further in section 4.1.3.

Although heterogeneous, if leeway needs to be summarised in one homogeneous coefficient it can be done by studying the relationship between leeway and wind speed similarly to (Allen and Plourde, 1999; Breivik et al., 2011). The linear regression slope (homogeneous leeway rate), correlation, R^2, standard error and confidence interval are reported in table 4.3.

Table 4.3: Leeway rate homogeneous representation across the sample as a function of wind speed, following Breivik et al. (2011)'s approach. All results are reported with two decimal digits.

Component	**Slope (%)**	S_e	**CI**	R^2	**N**
Downwind	1.69	0.02	[1.3, 2.1]	0.30	162
Crosswind	0.01	0.01	[0.01, 0.03]	0.00	162

When analysing the entire dataset, only the downwind component of leeway is statistically significant. It is less than 2%, confirming the overall low direct wind-drag of objects in the region when they are treated homogeneously as a simplification.

4.1.3 Leeway heterogeneity

Following Duhec et al. (2015)'s classification of fisheries' floating plastic, objects can be divided into "low windage (e.g., fishing nets and small plastic fragments), medium windage (e.g., polystyrene and partially filled PET bottles), or high windage (e.g., unfilled PET bottles and fishing buoys)" (Duhec et al., 2015). The authors chose coefficients of 1, 3 and 5% respectively. In this study, classification is performed on leeway rate and one more category is added, for a total of four: 0-1%, 1-2%, 2-4% and >4%. The derived leeway vectors can be distributed across these classes to gain more information on the distribution across the sample. Excluding measurement error, and other neglected signals such as inertia, this classification, displayed in figure 4.7a, can give insights leeway rate differences across objects for future work that could link leeway rates to object types. Other then the magnitude, objects' leeway angle of deflection is another important classifier that may be dependent on object type. Items that are subject to positive downwind leeway are plotted in 4.7b, inspired from Breivik et al. (2011)'s visualisation of different objects' measured leeway. Such items account for 82% of the sample.

Overall, almost half (45.7 %) of the tracked floating plastic is subject to null to low leeway (0-2%), with the almost equivalent quantity (40.1 %) experiencing medium leeway and less than 15% (14.2%) subject to high leeway. Almost half (44.4 %) of the sample's leeway is at a deflection angle smaller than 30°, whilst approximately a quarter (24.6 %) of the sample experiences a leeway between 30 and 60° with respect to the wind vector. Only a small portion of the sample (11.1 %) experiences drift almost perpendicularly to the right of the wind direction. These items experience weak leeway and could be deflected through Ekman transport due to a long vertical profile, depending on the prevalence of the leeway vector with respect to the total displacement vector. Following these results and based on Klink et al. (2022)'s hypothesis on windage's size dependency, an attempt to find a correlation between item size and leeway rate was conducted but resulted in a non statistically significant relation.

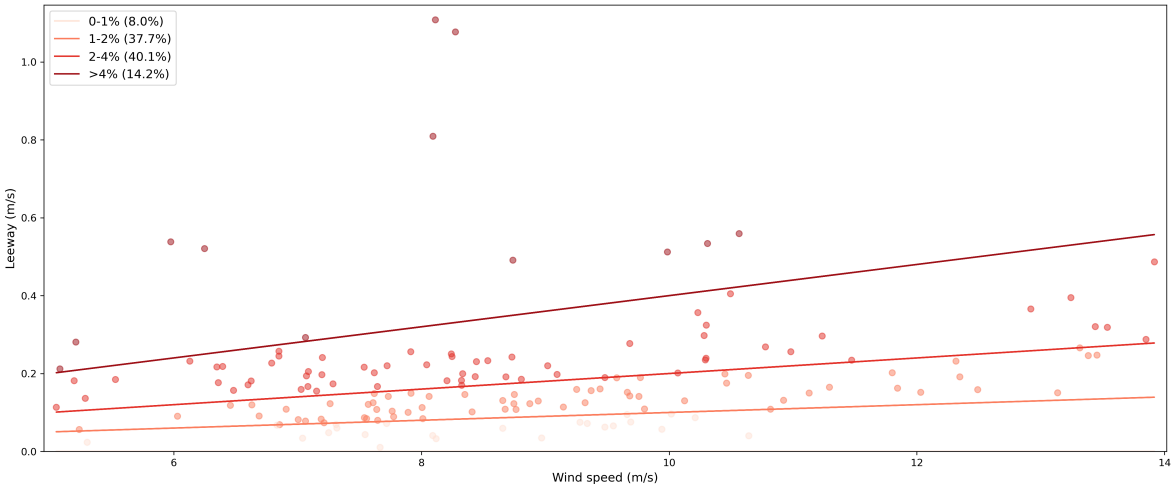

(a) Classification of leeway speed as 0-1%, 1-2%, 2-4% and 4% of wind speed, based on known leeway rates of fisheries' floating plastic (Duhec et al., 2015).

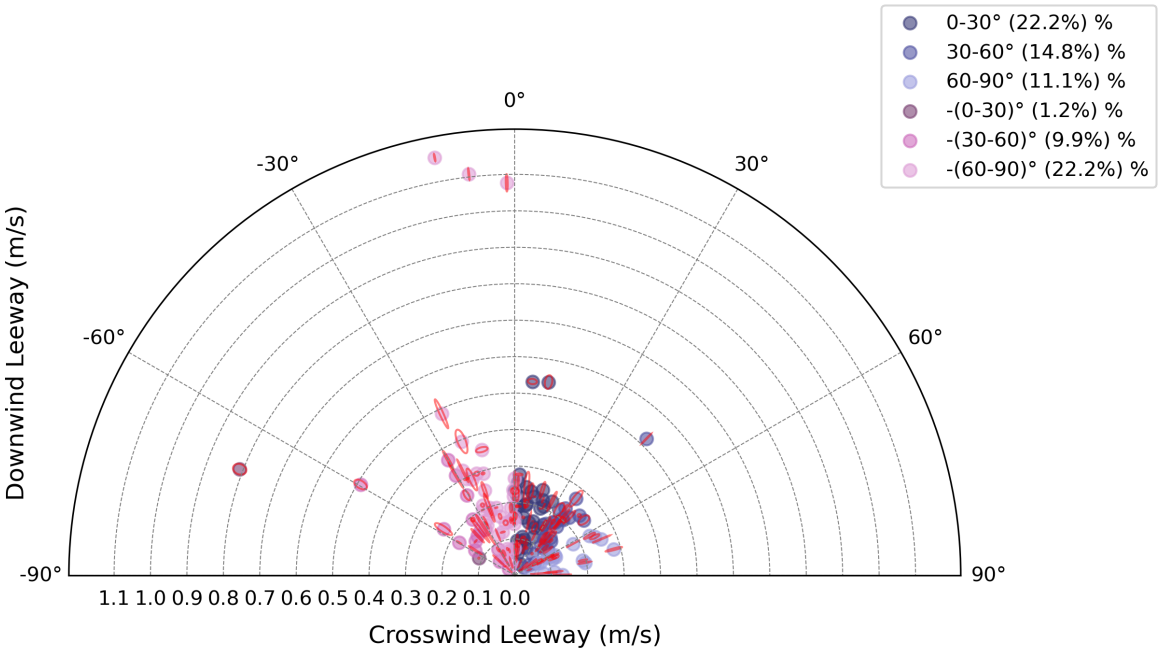

(b) Classification of leeway based on its magnitude and angle of deflection with respect to the wind vector following Breivik et al. (2011)'s approach. Red ellipses are the Montecarlo-computed standard deviations.

Figure 4.7: Leeway classification based on magnitude and angle of deflection with respect to the wind vector.

4.2 Spatial distribution

4.2.1 Density fronts

The most recent advancements on the importance of meso- and submesoscale structures on the heterogeneity of floating plastic in the GPGP were stated in section 2.1.4. Here, a qualitative analysis is conducted on the NPM5 dataset, by applying the theory on in situ observations of floating plastic densities, obtained from the shipboard GoPro cameras (section 3.1), and thermosalinograph-measured surface water density (section 3.2.5). The number of detected items is expressed as the total detections for each 1 km segment of the transect, omitting the second dimension for simplicity (which is constant over time and can be computed from the camera field of view applying de Vries et al. (2021)'s formulas). Hence, information on floating plastic accumulation is at 1 km resolution.

Supporting data from the operational Mercator global ocean analysis and forecast system is used to derive 2D relative vorticity, divergence and density data, as described in section 3.2.5. Figure 4.8 displays the spatio-temporal distribution of the detected floating plastic over the NPM5 campaign transect, superimposed on a color-map of the ratio between surface relative vorticity and Coriolis frequency ($R_o = \frac{\zeta}{f}$), contour-map of the density isolines and quiver-map of the flow field. Relative vorticity, in combination with flow field information, highlights the presence of eddies (Kumar et al., 2023).

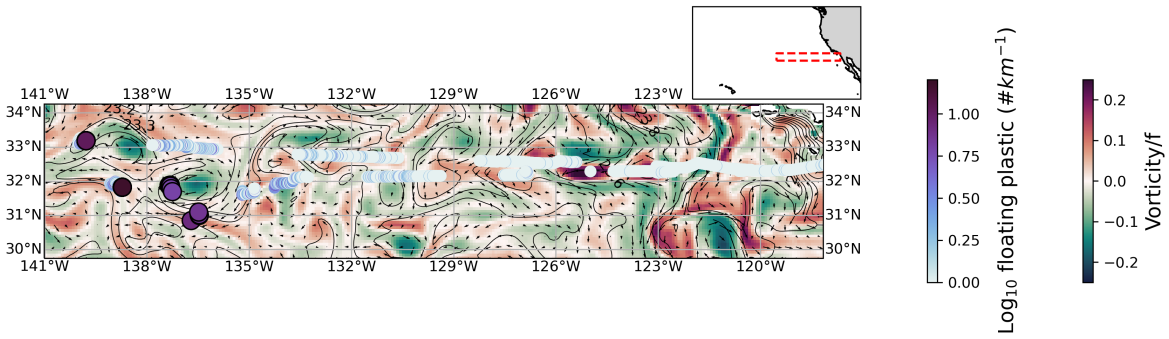

Figure 4.8: Map displaying floating plastic and surface flow within the domain of the NPM5 campaign. The scatter-plot displays the 1 km sections of the transect where the shipboard GoPro was active. The scatter-plot's color-map is the number of detected floating plastic per kilometer of transect in logarithmic scale. Sections with more than 5 detected items per kilometer have larger point sizes. The color-map is the time-averaged ratio between surface relative vorticity and Coriolis frequency over the campaign (data from Copernicus Marine Service (2023)). The quiver-plot is the surface flow-field and the contour-plot are the 0.2 km/m^3 density anomaly isolines.

In Figure 4.8, the number of detected floating plastic per kilometer increases as the ship approaches the gyre, and accumulation peaks in a region of higher mesoscale activity than the surrounding (31-34°N,136-140°W). Four areas of high accumulation can be identified from the figure, along the edges of two anticyclonic mesoscale structures. This region coincides with the anticyclonic activity spotted in November 2022 during the operational campaign (figure 4.2), suggesting the presence of a stationary or quasi-stationary structure. In this region $R_o = O(0.1)$, likely due to the lack of information at the smaller scales than 1/12°.

Over the campaign the median number of detected floating plastic per kilometer of transect is 0 (#/km), the mean is 0.43 (#/km) and the maximum is 15 (#/km). Within the above described region of higher mesoscale activity, the median is 1 (#/km), the mean is 2.69 (#/km) and the maximum is 10 (#/km). Therefore, the average number of detected items per kilometer is over 6 times higher around the two mesoscale anticyclonic structures than the entire transect. Nonetheless, this result may be influenced by the fact that this region is the inner-most location of the transect with respect to the gyre.

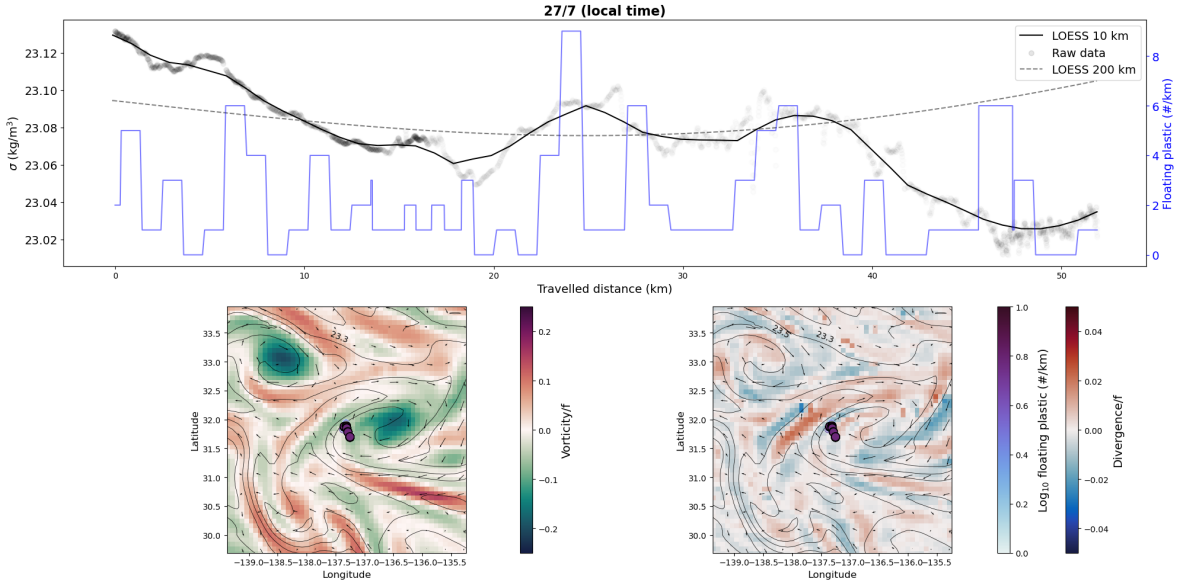

Figure 4.9: Map displaying floating plastic and surface flow on 27/07/22 (local time). a) On top, the thermosalinograph-derived density data is plotted along the transect, starting from 0 km at the start of the day. Raw density data at 1 minute resolution, 10 km and 200 km smoothed are plotted in black. The number of detected floating plastic at 1 km resolution is plotted in blue. b) The bottom left plot is equivalent to figure 4.8. c) The bottom right plot replaces the relative vorticity data with surface divergence.

Three of the high accumulation areas have available, continuous thermosalinograph data and are investigated in further detail. However, only two are displayed and discussed here (see appendix C for more). Figures 4.9 and 4.10 (as well as figure C.1) display the time-series of the thermosalinograph-derived density anomaly, σ, as well as the cropped region of interest from figure 4.8 and an additional figure including surface divergence.

Figure 4.9 shows data from the second day for highest mean daily detected items per kilometer, with median of 1 (#/km), mean of 1.87 (#/km) and maximum of 9 (#/km). The plotted data is a section of the day where thermosalinograph signal is not noisy and shows a high concentration (average is fourfold the campaign's) along the edge of a mesoscale anticyclone. The thermosalinograph data shows two coinciding peaks of floating plastic and density. The density peaks coincide with the frontal regions of convergence. The frontal line can be spotted by the two compressed isolines on the western section of the detected floating plastic. At the peaks, the denser flow downwells according to the theory (D'Asaro et al., 2018) and floating

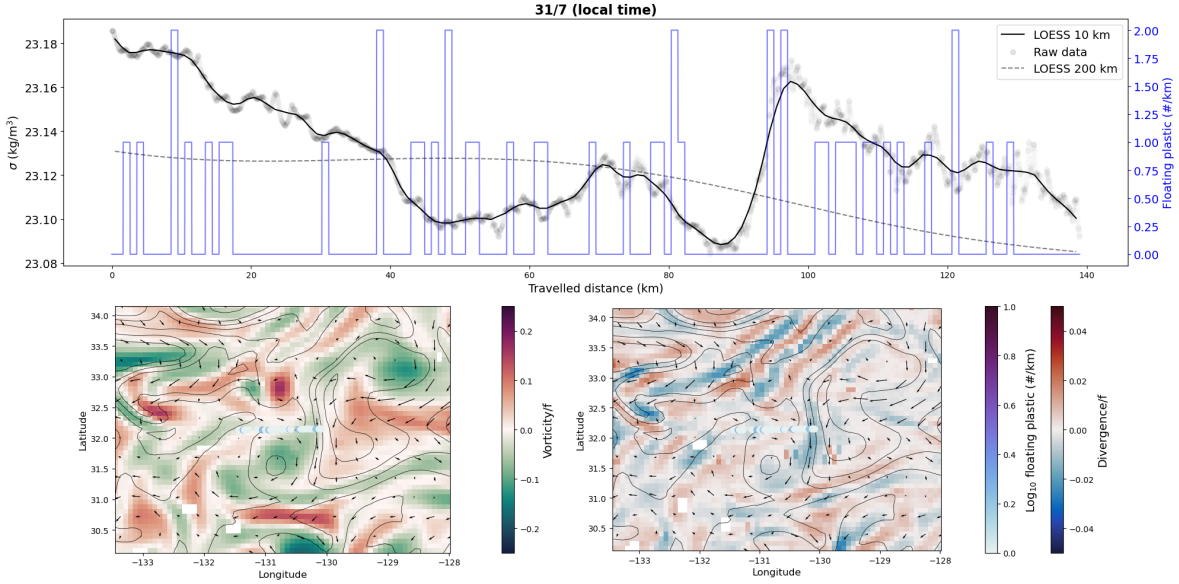

Figure 4.10: Map displaying floating plastic and surface flow on 31/07/22 (local time). The plot is in the same format as figure 4.9.

material accumulates, like described in section 2.1.4. Figure 4.10 displays a region with lower mean floating plastic than the campaign's, with median of 0 (#/km), mean of 0.29 (#/km) and maximum of 2 (#/km), but with a noticeable mesoscale density front of approximate gradient 0.01 kg/ (m^3km) over 10 km. The front coincides with the longest area of higher floating plastic accumulation compared to the surrounding. The number of detections is however, only 2 #/km.

Chapter 5

Discussion

5.1 Leeway

Results show the non-negligible role of leeway in the transport of floating plastic in the North-West region of the GPGP, as current-driven transport is unable to explain more than half of the variance of measured floating plastic transport. The downwind component of the leeway has been found to be statistically significant in the investigated wind regimes (> 5 m/s). A downwind leeway rate of 1.69 %, with confidence interval [1.3 %,2.1 %], is the most representative for the detected items. Furthermore, leeway increases the variability in the deflection angle of plastic transport with respect to surface currents' direction. Only 43.5 % of items have an angle of deflection smaller than 30° in high wind regimes (> 5 m/s), compared to 65.9 % in low wind (< 5 m/s). Additionally, results show evident heterogeneity in the importance of leeway across items, as 45.7 % of the tracked floating plastic is subject to null to low leeway (0-2%), 40.1 % to medium leeway (2-4%) and 14.2% to high leeway. Although this is only a preliminary result that necessitates further information on tracked objects' characteristics, it is likely that such heterogeneity in leeway confirms the variety of floating plastic types in the GPGP.

According to the model results presented by Lebreton et al. (2018), the GPGP is primarily composed of objects with low or no windage coefficient. Although direct comparison between windage and leeway rates is not possible, as the leeway includes both windage and wave-induced drift, the computed downwind leeway rate of 1.69 % suggests that, on average, tracked items experience null to low leeway. The agreement of the results with Lebreton et al. (2018)'s is enhanced if Clarke and Gorder (2018)'s parametrisation of wind-waves Stokes drift as 1 % of the 10 m wind is applied. If this were to be applicable, the computed windage would be below 1%. Nonetheless, this assumption neglects object-specific wave-induced drift, which has been found to be an important factor in theory and lab experiments (Alsina et al., 2020; Di Benedetto et al., 2022; Santamaria et al., 2013; Westerkamp et al., 2023). Furthermore, Lebreton et al. (2018) recognized that their sampling techniques may have underestimated the amounts of higher windage debris passing through the GPGP due to the short time

window. The heterogeneous leeway rates found across the sample in this study may confirm Lebreton et al. (2018)'s sampling underestimation of higher windage debris passing through the GPGP. According to Klink et al. (2022), wind has a more significant impact on larger particles compared to smaller microplastics. This is because larger particles have an increased surface area and are more likely to float at the surface due to their higher rising velocity. In the present study, items detected are larger than 0.15 m and on average, experience non-null wind forcing. This may be in agreement with Klink et al. (2022), however, no statistically significant correlation between leeway rate and size is found in this study. There are two potential reasons for this outcome. Firstly, the sample has a relatively narrow size distribution (section 4.1). Additionally, the heterogeneity of density and shape across different sizes also affects leeway rates (Breivik et al., 2011; Klink et al., 2022). Overall, the hypothesis that the observed heterogeneity in leeway may be due to the individual object's characteristics, although object-specific information is missing in this sample (except for size), is in line with the field results from Breivik et al. (2011) and van der Mheen et al. (2020), as well as the modelling outputs from Maximenko et al. (2018). Finally, modelling studies on the dispersion of floating material have started to adopt non-homogeneous windage coefficients in Lagrangian simulations Ruiz et al. (2022), confirming the importance of further research and validation on the influence of object-specific characteristics on their leeway rate.

Overall, results show that, although surface currents drive the large scale accumulation of floating plastic in the GPGP through Ekman transport, they are unable to explain over half of the variance in transport of the items in the sample on their own (research question 1). Additionally, conclusions on the proportion of floating plastic in the GPGP that is transported solely by surface-currents remain inconclusive, due to the inability to distinguish between objects that are trapped in the gyre and others that are travelling through. It is not to exclude that some objects may reside in the patch when meteorological conditions are calmer and escape in rougher weather, creating a seasonal dependence in the distribution within the GPGP. The observed behaviour of objects across the sample is therefore more complex than only surface currents-driven, primarily due to the influence of leeway. Leeway is a non-negligible component of floating plastic transport in the region, both in terms of speed and deflection angle with respect to the surrounding water (research question 2). Furthermore, there is clear heterogeneity in leeway rates across the sample and a single coefficient may unable to explain each object's wind influence on transport (research question 3). Although the findings mostly align with the existing literature, it is crucial to exercise caution when interpreting the results due to the various limitations acknowledged in this study. The main limitations stem from both the quality and size of the collected data, alongside potential errors introduced by the chosen methodology. Besides the sensitivity of the projection technique, as evaluated through the Monte Carlo analysis in chapter 3, the primary sources of error are likely attributed to the GPS signal and the DVL surface current measurements.

5.1.1 DVL and GPS

The lack of precise information regarding the DVL backscatter depth (Taudien, 2018) imposes restrictions on the precision of the calculated leeway. In contrast to the wind and wave data, preliminary quality checks did not reveal a significant correlation between DVL-derived surface

currents and data-assimilated model outputs from Copernicus Marine Service (2023). The lack of strong correlation, however, is influenced by many factors, other than the instrument's precision. Firstly, submesoscale currents which are not resolved in the models (McWilliams, 2016). Secondly, GPS error Peters and Skop (1996), and thirdly the influence of the wind drift on surface currents van der Mheen et al. (2020). Finally, a median deflection angle of 90° between the measured currents and the wind direction (figure B.2) could be an indicator of deeper DVL backscatter in the Ekman spiral, or depth-integrated measurements. The influence of this factor is pivotal in shaping the overall conclusions regarding the significance of leeway as a transport mechanism. Therefore, it necessitates further investigation using alternative in situ measurement devices, such as an ADCP, along with supplementary analyses. For now, this limitation implicates that the derived leeway angle and leeway speed are to be interpreted with caution. The negative downwind leeway measured on certain items (figure 4.5) and the low correlation between floating plastic transport and surface current in low wind regimes (table 4.1) could be justified by this factor. For now, a small magnitude, negative downwind signal is assumed to be an item that experiences no leeway.

5.1.2 Camera unknowns

This study is the first application of Schwendeman and Thomson (2014)'s projection method to derive velocities of floating debris. Sensitivity to varying wave conditions and other error sources have been studied in section 3.4.1. Nonetheless, measurement errors are still unclear, and it is likely that the input parameters in the Monte Carlo analysis may not follow a normal distribution as assumed (Nieto-Reyes, 2021). Hence, caution is needed particularly when inferring results from the data from mid October onward, due to a different camera setup and higher significant wave height.

5.1.3 Analysis framework

Additional limitations may arise from the analysis framework adopted in chapter 4. Following the definition given by Breivik et al. (2011), if results on leeway want to be generalised, wind speed should be taken as 10 minute mean, replacing the currently utilised median over the tracking time window, to avoid influence of short-lived wind gusts and inertia. Especially if the long-term objective is to define a standardized procedure for simplifying the drift properties of floating plastic to a set of coefficients to be incorporated into Lagrangian simulations. Additionally, the wind regimes filter (> 5 m/s), applied previous to the analysis in chapter 4, may exclude items that experience high leeway speed in the low wind regime that is discarded. From visual inspection, several items with leeway rate above 4% could be missed, altough uncertainty on the precision of these measurements is higher due to the smaller signal to noise ratio (section 4.1).

The assumed linearity between leeway speed and wind speed may not necessarily hold, especially when including wave effects (Breivik et al., 2011). Additionally, statistical limitations associated with the use of a constrained regression line are higher errors (by mathematical definition) than an unconstrained regression (Breivik et al., 2011) and may be more biased by measurement inaccuracies. Other factors that are not taken into account are state changes to the objects' conditions over the tracking window such as capsizing and rotating (Breivik

et al., 2011). To be properly addressed, these effects would, however, require longer tracking times than the ones available in this study.

5.1.4 Stokes drift

In section 2.1, the relationship between wind waves-induced Stokes drift and wind drag was conceptualised. Both physical mechanisms have been included in the commonly used term *leeway*, neglecting the role of swell waves-induced drift. Future research should attempt to separate the Stokes drift and the windage component. Two-dimensional wave measurements that work in mixed wave regimes would be needed.

The importance of Stokes drift remains the biggest unknown in the drift computations of this study (excluding measurement errors). Preliminary investigations on the detection of Stokes drift signal in the DVL measurements (by conducting correlations between the standard deviation of DVL-derived surface currents and X-band-derived significant wave height for different multiples of wave period) were inconclusive. It is likely that the signal is not included in the DVL measurement, as the device is unable to detect orbital motion at the surface, but lower in the water column where the signal is weaker (Stokes, 1847). Nonetheless, if the Stokes drift is included, leeway rates may have been underestimated.

Overall, further investigation is needed to draw wider conclusions on the role of wind-induced transport and hence, on the size of the GPGP (Lebreton et al., 2018). At the same time, results from this study emphasise the importance to include non-conform windage parameters in Lagrangian simulation.

5.2 Density fronts

A qualitative analysis on the distribution of detected floating plastic from shipboard GoPro footage (NPM5) over a period of two weeks shows possible accumulation in areas of higher mesoscale activity, particularly at the edge of anticyclones. Whilst on a larger scale, regions of stronger mesoscale activity may determine the gradients of average concentration (figure 4.8), figures 4.9 and 4.10 display the likely importance of density fronts as accumulation structures, creating heterogeneity at the small scale. Additionally, visual correlation between frontal areas of higher surface density and accumulation of floating plastic is found in two instances (figures 4.9 and 4.10).

Accumulation of floating material along the frontal area of denser water mass is suggested in other studies (D'Asaro et al., 2018; Hajbane et al., 2021), especially at the submesoscale. There, the stronger convergence and vorticity (D'Asaro et al., 2018) lead to higher accumulation rates than the ones found in this study. The observed higher concentrations of floating plastic along the edge of mesoscale anticyclonic structures could be in agreement with the intense vertical motions found by Xiu et al. (2022), as well as the accumulation of chlorophyll found by Liu et al. (2017). It's possible that there, higher rates of attraction are induced by ageostrophic currents (Liu et al., 2017), although lack of sufficiently resoluted data limits its conclusions in this case. Although accumulation of floating material along eddy edges is

recorded in the literature (Liu et al., 2017; Xiu et al., 2022), there remains controversy on whether fronts in anticyclonic structures are associated with convergence zones (McWilliams, 2016), like the cyclonic counterparts (D'Asaro et al., 2018).

Despite some promising preliminary results, with two episodes where floating plastic accumulation along density fronts is higher than in the surrounding area (research question 4), no clear conclusions can be drawn from this analysis due to several limitations. The accuracy of the floating plastic detections remains questionable, as it is likely that the measuring device is influenced by meteorological conditions, such as sun glare, shadows and white caps (de Vries et al., 2021). Additionally, the fact that optical data can only be obtained in the presence of sunlight impedes a continuous data collection. Although the objective of the research campaign was, amongst others, to detect accumulation fronts of floating plastic, sampling along fronts is complicated in practice, since the boundaries at fronts curve and meander (Hajbane et al., 2021). This factor could lead to a conservative estimate of total detected floating plastic. Furthermore, the lack of accompanying high resolution models, such as in the study from Xiu et al. (2022), limit the understanding of mechanisms at the submesoscale. Although plausible that the region in this analysis presents weak submesoscale activity, the small order of magnitude of the Rossby number computed from the Global Ocean Physics Analysis and Forecast at 1/12° (Copernicus Marine Service, 2023) is likely due to the inadequacy of extracting this information from such data, as information at the smaller scales is missing.

Overall, the science of submesoscale fluid dynamics is a young field, with many unknowns, both in the modelling and sampling (McWilliams, 2016). Consequently, it is not surprising that uncertainty and disagreement remain.

Chapter 6

Conclusion

The primary objective of this study was to use in situ observations to investigate the role of non-resolved submesoscale transport mechanisms on floating plastic in the GPGP, with a focus on leeway and density fronts. For such analysis, a PTV technique was developed and applied to shipboard GoPro data. It was validated firstly, by conducting a Monte Carlo analysis to assess the variability of the derived velocities and secondly, comparing results with the ones obtained by applying the same technique on drone data, over areas of overlapping footage.

The results demonstrate the heterogeneity of leeway rates among floating objects and their potential impact on the distribution of plastic debris in the gyre. Moreover, the role of density fronts as relevant factors in plastic accumulation requires further investigation. While this study provides insights into the transport of floating plastic, it is not without limitations. For instance, the analysis is based on shipboard camera data, which may not capture the full extent of plastic distribution nor measure its displacement with sufficient accuracy.

Future research could explore the integration of various data sources, including drone imagery, ADCP and an inertial measurement unit, to enhance the accuracy of plastic tracking. Nonetheless, the operational implementation of the PTV technique using shipboard cameras presents a cost-effective and practical approach for analyzing plastic movement and distribution in areas lacking other scientific measurements. In the way forward, collaborative efforts between diverse fields such as computer science, oceanography, and environmental science will be essential in addressing the complexities of plastic pollution and developing effective solutions. By combining insights from various disciplines, a better understanding of plastic transport could contribute to the development of more accurate models for predicting the distribution and accumulation of floating plastic both in the GPGP and globally.

In conclusion, this study underlines the significance of non-resolved submesoscale transport mechanisms in shaping the fate of floating plastic in the ocean. It opens up new avenues for future research and emphasizes the need for multidisciplinary approaches to tackle the

pressing issue of plastic pollution in marine environments.

Appendix A

Monte Carlo analysis

Results from the Montecarlo experiments applied on the operational dataset for different sea states are reported in this appendix. Both the Montecarlo sea surface projection and the derived velocity variance are plotted. The velocity variance is coupled with the operational dataset, with a value assigned based on the sea state measured from the X-Band radar at that moment and it is used as a filter to remove trajectories with $\hat{\sigma}_{\hat{\mathbf{u}}} > 0.1$ m/s.

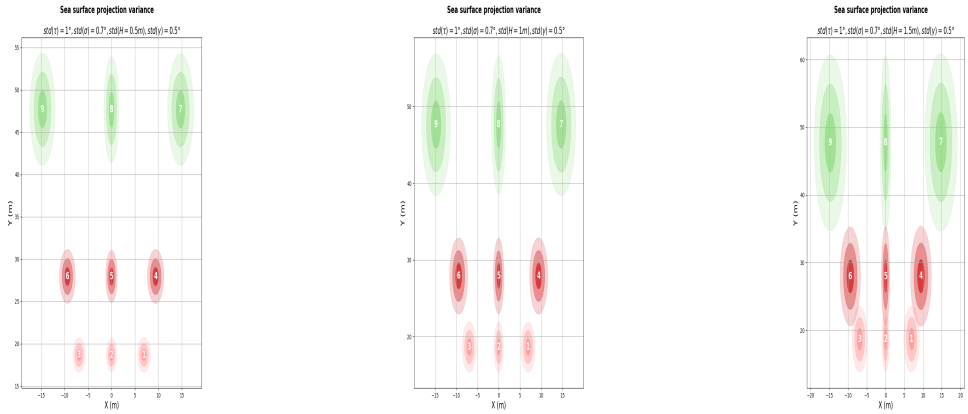

(a) SWH = 1 m (b) SWH = 2 m (c) SWH = 3 m

Figure A.1: Operational campaign sea surface projection variance for different sea states. As the wave height gets larger, so do the uncertainties in the projection.

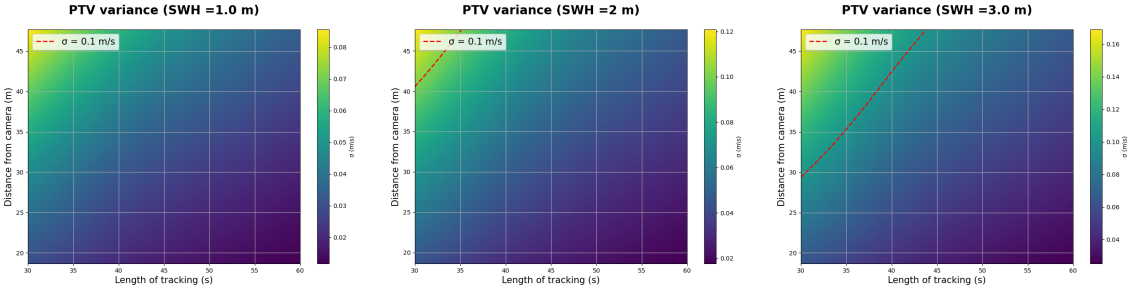

(a) SWH = 1 m (b) SWH = 2 m (c) SWH = 3 m

Figure A.2: Operational campaign PTV variance for different sea states. As the wave height gets larger, so do the uncertainties in the velocity derivation.

Appendix B

Leeway results

In figure B.1 the distribution of the down- and crosswind component of the leeway for each object is plotted over time. Only the objects tracked when 10 meter $u_w > 5$ m/s as described in section 4.1.2.

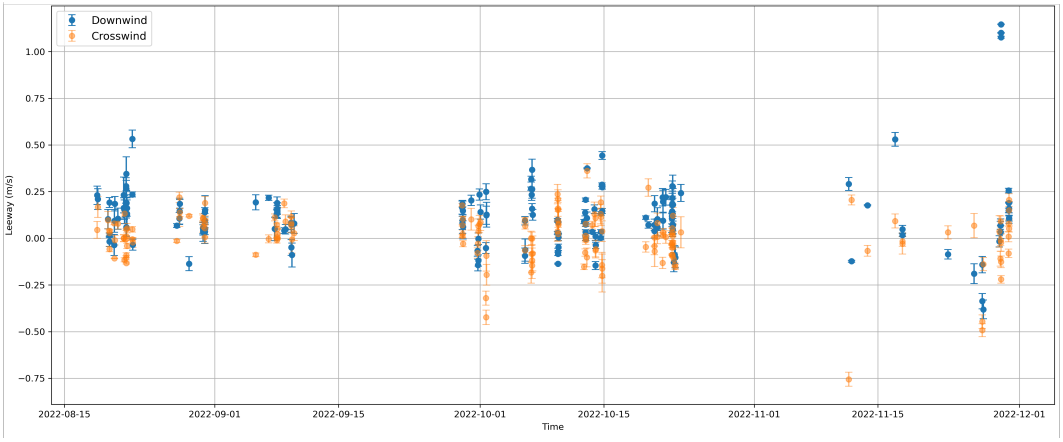

Figure B.1: Time distribution of cross and downwind components of leeway. Error bars are obtained from the Montecarlo results. Items are spread non-homogeneously over time due to the filter on wind speed and to the non-continuity of field measurements. Variance of downwind leeway is higher than crosswind.

In figure B.2 the distribution of the down- and crosswind component of the leeway for each object are plotted.

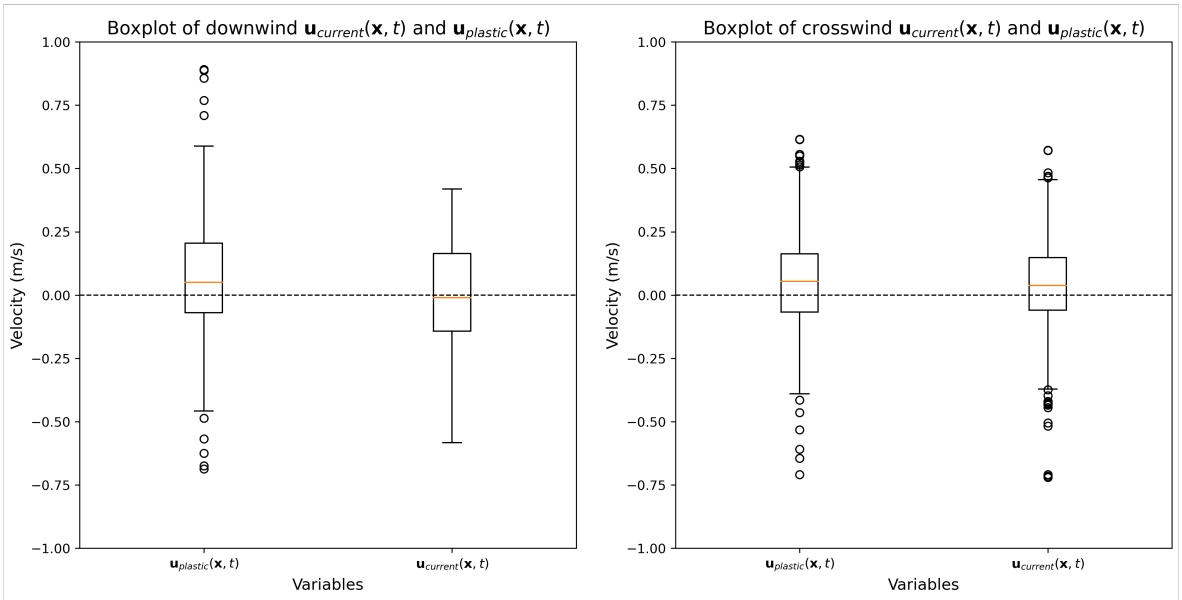

Figure B.2: Distribution of cross and downwind components of plastic transport and surface current as boxplot. The sample's downwind leeway is a positive, statistically significant signal. The median current is deflected at a 90° angle with respect to the wind direction.

Appendix C

Fronts results

Although a less clear structure is identifiable in figure C.1, peaks of floating plastic detections mostly coincide with the sections of the transect where the potential density gradient is highest, or within a few km.

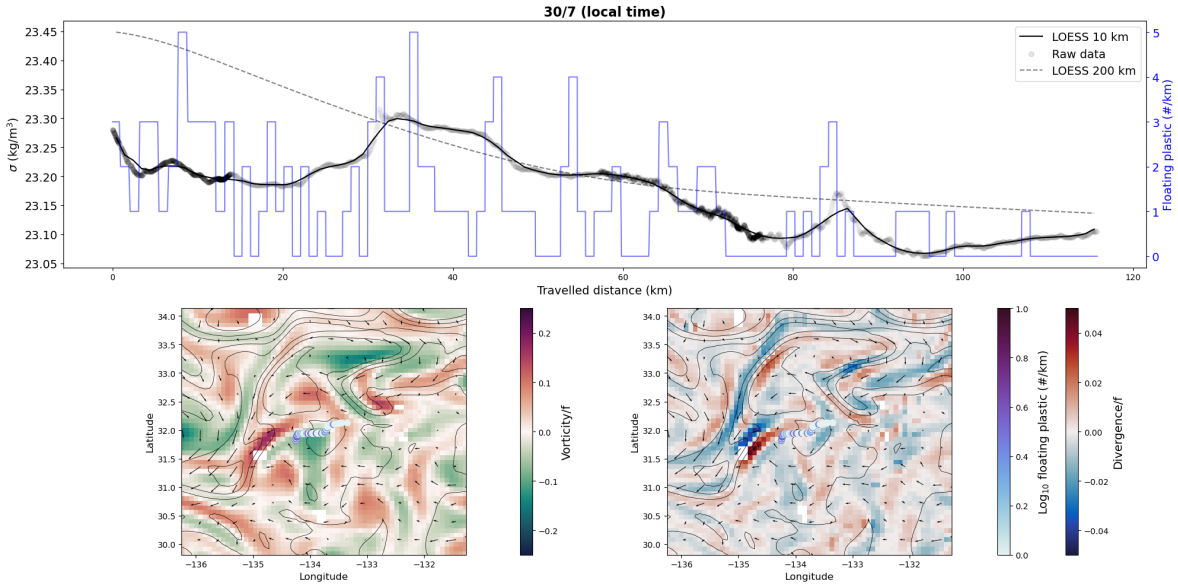

Figure C.1: Map displaying floating plastic and surface flow on 30/07/22 (local time). The plot is in the same format as figure 4.9

Bibliography

Allen and Plourde. Review of leeway: Field experiments and implementation, 1999. URL `https://apps.dtic.mil/sti/pdfs/ADA366414.pdf`.

M. R. Allshouse, G. N. Ivey, R. J. Lowe, N. L. Jones, C. J. Beegle-Krause, J. Xu, and T. Peacock. Impact of windage on ocean surface lagrangian coherent structures. *Environmental Fluid Mechanics*, 17(3):473–483, dec 2016. doi: 10.1007/s10652-016-9499-3.

W. R. Alpers, D. B. Ross, and C. L. Rufenach. On the detectability of ocean surface waves by real and synthetic aperture radar. *Journal of Geophysical Research*, 86(C7):6481, 1981. doi: 10.1029/jc086ic07p06481.

J. M. Alsina, C. E. Jongedijk, and E. van Sebille. Laboratory measurements of the wave-induced motion of plastic particles: Influence of wave period, plastic size and plastic density. *Journal of Geophysical Research: Oceans*, 125(12):e2020JC016294, 2020. doi: https://doi.org/10.1029/2020JC016294.

R. E. Andrews. What causes the trade winds and the westerlies? *School Science and Mathematics*, 56(7):572–574, 1956. doi: 10.1111/j.1949-8594.1956.tb13140.x.

A. R. Aves, L. E. Revell, S. Gaw, H. Ruffell, A. Schuddeboom, N. E. Wotherspoon, M. LaRue, and A. J. McDonald. First evidence of microplastics in antarctic snow. *The Cryosphere*, 16(6):2127–2145, 2022. doi: 10.5194/tc-16-2127-2022.

B. Barceló-Llul, K. Drushka, and P. Gaube. Lagrangian reconstruction to extract small-scale salinity variability from smap observations. *Journal of Geophysical Research: Oceans*, 126, 3 2021. doi: 10.1029/2020JC016477.

I. M. Belkin, P. C. Cornillon, and K. Sherman. Fronts in large marine ecosystems. *Progress in Oceanography*, 81:223–236, 4 2009. doi: 10.1016/j.pocean.2009.04.015.

G. Blewitt. *Geodetic Applications of GPS*, chapter Basics of the GPS Technique: Observation Equations. Swedish Land Survey, 1997.

Y. Breivik, A. A. Allen, C. Maisondieu, and J. C. Roth. Wind-induced drift of objects at sea: The leeway field method. *Applied Ocean Research*, 33:100–109, 4 2011. doi: 10.1016/j.apor.2011.01.005.

F. Bünning, B. Huber, A. Schalbetter, A. Aboudonia, M. Hudoba de Badyn, P. Heer, R. S. Smith, and J. Lygeros. Physics-informed linear regression is competitive with two machine

learning methods in residential building mpc. *Applied Energy*, 310:118491, 2022. doi: https://doi.org/10.1016/j.apenergy.2021.118491.

C. M. Callbeck, G. Lavik, L. Stramma, M. M. M. Kuypers, and L. A. Bristow. Enhanced nitrogen loss by eddy-induced vertical transport in the offshore peruvian oxygen minimum zone. *PLOS ONE*, 12(1):1–18, 01 2017. doi: 10.1371/journal.pone.0170059.

D. B. Chelton, M. G. Schlax, and R. M. Samelson. Global observations of nonlinear mesoscale eddies. *Progress in Oceanography*, 91(2):167–216, 2011. doi: https://doi.org/10.1016/j.pocean.2011.01.002.

X. Chen and G. Chen. Quantifying the degree of eddy quasi-geostrophy by generalizing rossby deformation. *Journal of Geophysical Research: Oceans*, 128(6), 2023. doi: 10.1029/2023jc019652.

A. J. Clarke and S. V. Gorder. The relationship of near-surface flow, stokes drift and the wind stress. *Journal of Geophysical Research: Oceans*, 123:4680–4692, 7 2018. doi: 10.1029/2018JC014102.

A. Cohen and G. Migliorati. Optimal weighted least-squares methods, 2016.

J. Colen and E. B. Kolomeisky. Kelvin–froude wake patterns of a traveling pressure disturbance. *European Journal of Mechanics - B/Fluids*, 85:400–412, 2021. doi: https://doi.org/10.1016/j.euromechflu.2020.10.008.

Copernicus Marine Service. Global ocean physics analysis and forecast, 2023. URL `https://data.marine.copernicus.eu/product/GLOBAL_ANALYSISFORECAST_PHY_001_024/description`.

B. Cushman-Roisin and J.-M. Beckers. Introduction. In *International Geophysics*, International geophysics series, pages 3–39. Elsevier, 2011.

D. Dabiri and C. Pecora. *Particle Tracking Velocimetry*. 2053-2563. IOP Publishing, 2019. doi: 10.1088/978-0-7503-2203-4.

Ø. Ø. Dalheim and S. Steen. Uncertainty in the real-time estimation of ship speed through water. *Ocean Engineering*, 235:109423, 2021. doi: https://doi.org/10.1016/j.oceaneng.2021.109423.

R. de Vries, M. Egger, T. Mani, and L. Lebreton. Quantifying floating plastic debris at sea using vessel-based optical data and artificial intelligence. *Remote Sensing*, 13, 9 2021. doi: 10.3390/rs13173401.

M. H. Di Benedetto, L. K. Clark, and N. Pujara. Enhanced settling and dispersion of inertial particles in surface waves. *Journal of Fluid Mechanics*, 936:A38, 2022. doi: 10.1017/jfm.2022.95.

D. Dobler, T. Huck, C. Maes, N. Grima, B. Blanke, E. Martinez, and F. Ardhuin. Large impact of stokes drift on the fate of surface floating debris in the south indian basin. *Marine Pollution Bulletin*, 148:202–209, 2019. doi: https://doi.org/10.1016/j.marpolbul.2019.07.057.

T. Dracos. *Particle Tracking Velocimetry (PTV)*, pages 155–160. Springer Netherlands, Dordrecht, 1996. ISBN 978-94-015-8727-3. doi: 10.1007/978-94-015-8727-3_7.

A. V. Duhec, R. F. Jeanne, N. Maximenko, and J. Hafner. Composition and potential origin of marine debris stranded in the western indian ocean on remote alphonse island, seychelles. *Marine Pollution Bulletin*, 96(1):76–86, 2015. doi: https://doi.org/10.1016/j.marpolbul.2015.05.042.

E. A. D'Asaro, A. Y. Shcherbina, J. M. Klymak, J. Molemaker, G. Novelli, C. M. Guigand, A. C. Haza, B. K. Haus, E. H. Ryan, G. A. Jacobs, H. S. Huntley, N. J. M. Laxague, S. Chen, F. Judt, J. C. McWilliams, R. Barkan, A. D. Kirwan, A. C. Poje, and T. M. Özgökmen. Ocean convergence and the dispersion of flotsam. *Proceedings of the National Academy of Sciences*, 115(6):1162–1167, 2018. doi: 10.1073/pnas.1718453115.

S. Emeis and M. Turk. *Comparison of Logarithmic Wind Profiles and Power Law Wind Profiles and their Applicability for Offshore Wind Profiles*, pages 61–64. 02 2007. doi: 10.1007/978-3-540-33866-6_11.

M. Eriksen, L. C. M. Lebreton, H. S. Carson, M. Thiel, C. J. Moore, J. C. Borerro, F. Galgani, P. G. Ryan, and J. Reisser. Plastic pollution in the world's oceans: More than 5 trillion plastic pieces weighing over 250,000 tons afloat at sea. *PLOS ONE*, 9(12):1–15, 12 2014. doi: 10.1371/journal.pone.0111913.

E. Fernández and R. D. Pingree. Coupling between physical and biological fields in the north atlantic subtropical front southeast of the azores. *Deep Sea Research Part I: Oceanographic Research Papers*, 43(9):1369–1393, 1996. doi: https://doi.org/10.1016/S0967-0637(96)00065-9.

S. Hajbane, B. Calmanovici, J. Reisser, A. Jolly, V. Summers, F. Ferrari, A. Ghadouani, and C. Pattiaratchi. Coastal garbage patches: Fronts accumulate plastic films at ashmore reef marine park (pulau pasir), australia. *Frontiers in Marine Science*, 8, 4 2021. doi: 10.3389/fmars.2021.613399.

P. E. Hamlington, L. P. V. Roekel, B. Fox-Kemper, K. Julien, and G. P. Chini. Langmuir–submesoscale interactions: Descriptive analysis of multiscale frontal spindown simulations. *Journal of Physical Oceanography*, 44(9):2249 – 2272, 2014. doi: https://doi.org/10.1175/JPO-D-13-0139.1.

H. Hewitt, B. Fox-Kemper, B. Pearson, M. Roberts, and D. Klocke. The small scales of the ocean may hold the key to surprises. *Nature Climate Change*, 12(6):496–499, 2022. doi: 10.1038/s41558-022-01386-.

W. Huang, X. Liu, and E. W. Gill. Ocean wind and wave measurements using x-band marine radar: A comprehensive review. *Remote Sensing*, 9(12), 2017. doi: 10.3390/rs9121261.

IUCN, Jun 2023. URL `https://www.iucn.org/resources/issues-brief/marine-plastic-pollution`.

W. G. Jacoby. Loess:: a nonparametric, graphical tool for depicting relationships between vari-

ables. *Electoral Studies*, 19(4):577–613, 2000. doi: https://doi.org/10.1016/S0261-3794(99)00028-1.

A. Johansen. Monte carlo methods. In P. Peterson, E. Baker, and B. McGaw, editors, *International Encyclopedia of Education (Third Edition)*, pages 296–303. Elsevier, Oxford, third edition edition, 2010. ISBN 978-0-08-044894-7. doi: https://doi.org/10.1016/B978-0-08-044894-7.01543-8.

M. Kaandorp, D. Lobelle, C. Kehl, H. A. Dijkstra, and E. van Sebille. *Closing the marine plastic mass budget Using observational data to inform numerical models*. 2023. doi: 10.33540/1583.

J. W. Kean and J. D. Smith. Form drag in rivers due to small-scale natural topographic features: 1. regular sequences. *Journal of Geophysical Research: Earth Surface*, 111, 12 2006. doi: 10.1029/2006JF000467.

P. Klein and G. Lapeyre. The oceanic vertical pump induced by mesoscale and submesoscale turbulence. *Annual review of marine science*, 1:351–75, 2009. URL `https://api.semanticscholar.org/CorpusID:13077374`.

D. Klink, A. Peytavin, and L. Lebreton. Size dependent transport of floating plastics modeled in the global ocean. *Frontiers in Marine Science*, 9, 7 2022. doi: 10.3389/fmars.2022.903134.

S. Kumar, C. Meneveau, and G. Eyink. Vorticity cascade and turbulent drag in wall-bounded flows: plane poiseuille flow, 2023.

L. J. Kunz. Transient attracting profiles in the great pacific garbage patch. In *EGU General Assembly 2023*. European Geosciences Union, 2023. doi: https://doi.org/10.5194/egusphere-egu23-12892,2023.

S. G. Kwak and J. H. Kim. Central limit theorem: The cornerstone of modern statistics. *Korean Journal of Anesthesiology*, 70(2):144, 2017. doi: 10.4097/kjae.2017.70.2.144.

J. LaCasce. Statistics from lagrangian observations. *Progress in Oceanography*, 77(1):1–29, 2008. doi: https://doi.org/10.1016/j.pocean.2008.02.002.

N. J. M. Laxague, T. M. Özgökmen, B. K. Haus, G. Novelli, A. Shcherbina, P. Sutherland, C. M. Guigand, B. Lund, S. Mehta, M. Alday, and J. Molemaker. Observations of near-surface current shear help describe oceanic oil and plastic transport. *Geophysical Research Letters*, 45(1):245–249, 2018. doi: https://doi.org/10.1002/2017GL075891.

L. Lebreton, B. Slat, F. Ferrari, B. Sainte-Rose, J. Aitken, R. Marthouse, S. Hajbane, S. Cunsolo, A. Schwarz, A. Levivier, K. Noble, P. Debeljak, H. Maral, R. Schoeneich-Argent, R. Brambini, and J. Reisser. Evidence that the great pacific garbage patch is rapidly accumulating plastic. *Scientific Reports*, 8, 12 2018. doi: 10.1038/s41598-018-22939-w.

L. Lebreton, S. J. Royer, A. Peytavin, W. J. Strietman, I. Smeding-Zuurendonk, and M. Egger. Industrialised fishing nations largely contribute to floating plastic pollution in the north pacific subtropical gyre. *Scientific Reports*, 12, 12 2022. doi: 10.1038/s41598-022-16529-0.

F. Liu, S. Tang, R. X. Huang, and K. Yin. The asymmetric distribution of phytoplankton in

anticyclonic eddies in the western south china sea. *Deep Sea Research Part I: Oceanographic Research Papers*, 120:29–38, 2017. doi: https://doi.org/10.1016/j.dsr.2016.12.010.

N. A. Malik, T. Dracos, and D. A. Papantoniou. Experiments in fluids particle tracking velocimetry in three-dimensional flows part ii: Particle tracking. *Experiments in Fluids*, 15: 279–294, 1993. doi: https://doi.org/10.1007/BF00223406.

N. Maximenko, J. Hafner, M. Kamachi, and A. MacFadyen. Numerical simulations of debris drift from the great japan tsunami of 2011 and their verification with observational reports. *Marine Pollution Bulletin*, 132:5–25, 7 2018. doi: 10.1016/j.marpolbul.2018.03.056.

D. J. McGillicuddy, A. R. Robinson, D. A. Siegel, H. W. Jannasch, R. Johnson, T. D. Dickey, J. McNeil, A. F. Michaels, and A. H. Knap. Influence of mesoscale eddies on new production in the sargasso sea. *Nature*, 394(6690):263–266, July 1998. doi: 10.1038/28367.

J. C. McWilliams. Submesoscale currents in the ocean. *Proceedings of the Royal Society A: Mathematical, Physical and Engineering Sciences*, 472:20160117, 5 2016. doi: 10.1098/rspa.2016.0117.

L. J. J. Meijer, T. van Emmerik, R. van der Ent, C. Schmidt, and L. Lebreton. More than 1000 rivers account for 80% of global riverine plastic emissions into the ocean. *Science Advances*, 7(18):eaaz5803, 2021. doi: 10.1126/sciadv.aaz5803.

J. Neter, M. H. Kutner, C. J. Nachtsheim, and W. Wasserman. *Applied Linear Statistical Models*. Irwin, 1996.

A. Nieto-Reyes. On the non-gaussianity of the height of sea waves. *Journal of Marine Science and Engineering*, 9(12), 2021. doi: 10.3390/jmse9121446.

M. Nikurashin and R. Ferrari. Global energy conversion rate from geostrophic flows into internal lee waves in the deep ocean. *Geophys. Res. Lett.*, 38(8), Apr. 2011.

OECD. *Global Plastics Outlook*. 2022. doi: https://doi.org/https://doi.org/10.1787/de747aef-en.

V. Onink, D. Wichmann, D. Wichmann, P. Delandmeter, and E. van Sebille. The role of ekman currents, geostrophy, and stokes drift in the accumulation of floating microplastic. *Journal of Geophysical Research*, 2019. doi: https://doi.org/10.1029/2018JC014547.

T. D. O'Brien, L. Lorenzoni, K. Isensee, and L. Valdés. What are marine ecological time series telling us about the ocean? a status report., 2017. URL `http://hdl.handle.net/1834/42096`.

N. J. Peters and R. A. Skop. Measurements of ocean surface currents from a moving ship using vhf radar. 1996.

A. A. Petty, M. C. Tsamados, and N. T. Kurtz. Atmospheric form drag coefficients over arctic sea ice using remotely sensed ice topography data, spring 2009–2015. *Journal of Geophysical Research: Earth Surface*, 122(8):1472–1490, 2017. doi: https://doi.org/10.1002/2017JF004209.

J. F. Price, R. A. Weller, and R. R. Schudlich. Wind-driven ocean currents and ekman transport. *Science*, 238(4833):1534–1538, 1987. doi: 10.1126/science.238.4833.1534.

Python library. Python random generator module, 2023. URL `https://docs.python.org/3/library/random.html`.

T. N. Quoc, P. D. Hieu, N. Q. Trinh, N. M. Huan, and D. V. Toan. Simulation for object drift forecast in the east vietnam sea by the leeway numerical method vietnam institute of seas and islands du van toan ministry of natural resources and environment of vietnam simulation for object drift forecast in the east vietnam sea by the leeway numerical method. 2013. URL `https://www.researchgate.net/publication/317958122`.

A. D. Rakotonirina, Y. Pham, B. Sainte-Rose, and T. van den Bremer. Numerical simulation of the wave-induced drift of floating marine plastic debris modeled as discrete particles. In *International Conference on Offshore Mechanics and Arctic Engineering*, volume 85925, page V007T08A008. American Society of Mechanical Engineers, 2022.

A. Reinsvold. Roll and pitch corrections for a shipboard anemometer, 2013. URL `https://digitalcommons.csbsju.edu/honors_theses/730`.

P. L. Richardson. Drifting in the wind: leeway error in shipdrift data. *Deep Sea Research Part I: Oceanographic Research Papers*, 44(11):1877–1903, 1997. doi: https://doi.org/10.1016/S0967-0637(97)00059-9.

M.-H. Rio and J.-F. Piollé. Globcurrent: Product format and content, 2015.

F. Roquet, G. Madec, T. McDougall, and P. Barker. Accurate polynomial expressions for the density and specific volume of seawater using the teos-10 standard. *Ocean Modelling*, 04 2015. doi: 10.1016/j.ocemod.2015.04.002.

I. Ruiz, A. Ana J., O. C. Basurko, and A. Rubio. Modelling the distribution of fishing-related floating marine litter within the bay of biscay and its marine protected areas. *Environmental Pollution*, 292:118216, 2022. doi: https://doi.org/10.1016/j.envpol.2021.118216.

F. Santamaria, G. Boffetta, M. M. Afonso, A. Mazzino, M. Onorato, and D. Pugliese. Stokes drift for inertial particles transported by water waves. *Europhysics Letters*, 102(1):14003, apr 2013. doi: 10.1209/0295-5075/102/14003.

M. Schwendeman and J. Thomson. A horizon-tracking method for shipboard video stabilization and rectification*. 2014. doi: 10.1175/JTECH-D.

G. G. Stokes. On the theory of oscillatory waves. *Transactions of the Cambridge Philosophical Society*, 8:441–455, 1847.

B. M. G. A. M. A. T. M. Z. E. Suaria, G. and S. Aliani. Dynamics of transport, accumulation, and export of plastics at oceanic fronts. *The Handbook of Environmental Chemistry*, pages 1–51, 2022. doi: 10.1007/698_2021_814.

H. Sugita. Monte carlo method, random number, and pseudorandom number. *MSJ Memoirs*, 25:14–133, 2011.

P. P. Sullivan and J. C. McWilliams. Frontogenesis and frontal arrest of a dense filament in the oceanic surface boundary layer. *Journal of Fluid Mechanics*, 837:341–380, 2018. doi: 10.1017/jfm.2017.833.

B. R. Sutherland, M. Di Benedetto, A. Kaminski, and T. van den Bremer. Fluid dynamics challenges in predicting plastic pollution transport in the ocean: A perspective. *Physical Review Fluids*, 8:070701, 7 2023. doi: 10.1103/PhysRevFluids.8.070701.

J. Y. Taudien. Doppler velocity log algorithms: Detection, estimation and accuracy. *The Graduate School College of Engineering*, 2018. URL `https://etda.libraries.psu.edu/files/final_submissions/17327`.

H. Tennekes. The logarithmic wind profile. *Journal of Atmospheric Sciences*, 30(2):234 – 238, 1973. doi: https://doi.org/10.1175/1520-0469(1973)030⟨0234:TLWP⟩2.0.CO;2.

The Ocean Cleanup, May 2023. URL `https://theoceancleanup.com/ocean-plastic/`.

The Ocean Cleanup. The ocean cleanup website, oceans section, n.d. URL `https://theoceancleanup.com/oceans/`.

R. Thompson, C. Moore, A. Andrady, M. Gregory, H. Takada, and S. Weisberg. New directions in plastic debris. *Science*, 310(5751):1117–1117, 2005. doi: 10.1126/science.310.5751.1117b.

H. L. Tolman. User manual and system documentation of WAVEWATCH III TM version 3.14. *Technical note, MMAB Contribution*, 276(220), 2009.

Ultralytics. Ultralytics/yolov5: Yolov5 in pytorch, n.d. URL `https://github.com/ultralytics/yolov5`.

UNESCO. A state of emergency, Feb 2021. URL `https://en.unesco.org/courier/2021-1/state-emergency#:~:text=Global%20warming%2C%20acidification%2C%20pollution%2C,of%20the%20planet%20at%20risk.`

T. S. van den Bremer and Breivik. Stokes drift. *Philosophical Transactions of the Royal Society A: Mathematical, Physical and Engineering Sciences*, 376, 1 2018. doi: 10.1098/rsta.2017.0104.

M. van der Mheen, C. Pattiaratchi, S. Cosoli, and M. Wandres. Depth-dependent correction for wind-driven drift current in particle tracking applications. *Frontiers in Marine Science*, 7, 2020. doi: 10.3389/fmars.2020.00305.

E. van Sebille, M. H. England, and G. Froyland. Origin, dynamics and evolution of ocean garbage patches from observed surface drifters. *Environmental Research Letters*, 7, 2012. doi: 10.1088/1748-9326/7/4/044040.

E. van Sebille, C. Wilcox, L. Lebreton, N. Maximenko, B. D. Hardesty, J. A. van Franeker, M. Eriksen, D. Siegel, F. Galgani, and K. L. Law. A global inventory of small floating plastic debris. *Environmental Research Letters*, 10(12):124006, dec 2015. doi: 10.1088/1748-9326/10/12/124006.

E. van Sebille, S. Aliani, K. L. Law, N. Maximenko, J. M. Alsina, A. Bagaev, M. Bergmann, B. Chapron, I. Chubarenko, A. Cózar, P. Delandmeter, M. Egger, B. Fox-Kemper, S. P. Garaba, L. Goddijn-Murphy, B. D. Hardesty, M. J. Hoffman, A. Isobe, C. E. Jongedijk, M. L. Kaandorp, L. Khatmullina, A. A. Koelmans, T. Kukulka, C. Laufkötter, L. Lebreton, D. Lobelle, C. Maes, V. Martinez-Vicente, M. A. M. Maqueda, M. Poulain-Zarcos, E. Rodríguez, P. G. Ryan, A. L. Shanks, W. J. Shim, G. Suaria, M. Thiel, T. S. V. D. Bremer, and D. Wichmann. The physical oceanography of the transport of floating marine debris. *Environmental Research Letters*, 15, 2 2020. doi: 10.1088/1748-9326/ab6d7d.

N. Villacieros-Robineau, M. Gilcoto, P. C. Pardo, and E. D. Barton. Wave regime and wave-current coupling in an upwelling–driven bay: Seasonal and inter-annual variability. *J. Geophys. Res. Oceans*, 126(11), nov 2021.

D. Westerkamp, A. D. Rakotonirina, and B. Sainte-Rose. Numerical simulation of the wave-induced drift of disc-shaped floating plastic debris. In *International Conference on Offshore Mechanics and Arctic Engineering*. American Society of Mechanical Engineers, 2023.

D. Wichmann, P. Delandmeter, and E. van Sebille. Influence of near-surface currents on the global dispersal of marine microplastic. *Journal of Geophysical Research: Oceans*, 124(8): 6086–6096, 2019. doi: https://doi.org/10.1029/2019JC015328.

P. Xiu, L. Guo, and W. Ma. Modelling the influence of submesoscale processes on phytoplankton dynamics in the northern south china sea. *Frontiers in Marine Science*, 9, 2022. doi: 10.3389/fmars.2022.967678.

E. Zambianchi, G. Suaria, S. Aliani, and I. Iermano. Marine litter in the mediterranean sea: an oceanographic perspective. 2014. doi: 10.13140/RG.2.1.2315.3760.

N. Zolotova, A. Kosyreva, D. Dzhalilova, N. Fokichev, and O. Makarova. Harmful effects of the microplastic pollution on animal health: A literature review. *PeerJ*, 10, 2022. doi: 10.7717/peerj.13503.